Utrecht University

Faculteit Bètawetenschappen

Measurement of feed-down D^{*+} mesons in Pb-Pb collisions at $\sqrt{s_{NN}} = 5.02$ TeV in centrality class $10 - 30\%$ using topological selections

Bachelor Thesis

W.P.G Meering

Study: Natuur- en Sterrenkunde

Supervisors:

Dr. A. Grelli
Institute for Subatomic Physics

PhD candidate S. Jaelani
Institute for Subatomic Physics

June 2018

Abstract

Quantum chromodynamics predicts that a few microseconds after the Big Bang the matter of our Universe was in a plasma state called Quark-Gluon Plasma (QGP), where quarks and gluons were deconfined and free to move. Heavy ion collisions at the Relativistic Heavy Ion Collider (RHIC) and Large Hadron Collider (LHC) create conditions which allow for this plasma state to form. The QGP created in Pb-Pb collisions lasts only for a few femtoseconds and is a few femtometers in size, therefore it can not be directly accessed. In order to study its properties, elementary particles are used as probes. Examples of such probes are charm and beauty quarks, that can be accessed by studying the D^{*+} meson. In Pb-Pb collisions D^{*+} mesons can be formed directly from a charm quark (prompt) or by decay of a B meson (feed-down), which itself is produced from a beauty quark. In particular being able to select a pure sample of D^{*+} mesons from beauty hadron decays would allow the interactions of the beauty quark with the quark-gluon plasma to be studied.

In this study topological selections aimed at the selection of feed-down D^{*+} are studied. Two sets of feed-down enhanced cuts (loose and tight) are reported for the topological variables: impact parameter kaon, impact parameter pion, normalised decay length XY and cosine pointing angle. These two sets of cuts are individually applied on ALICE Pb-Pb collision data ($\sqrt{s_{NN}} = 5.02$ TeV, centrality class 10-30%) and the results are analysed using invariant mass spectra, efficiency and prompt fraction.

The loose and tight feed-down enhanced cuts are determined by exploiting the different shapes of topological variable distributions. Resulting D^{*+} signals are measured for the loose cuts at transverse momentum between $4 - 24$ GeV/c and for the tight cuts between $2 - 8$ GeV/c. The prompt fractions of both the loose and tight feed-down enhanced cuts show an increase in feed-down contribution compared to the standard analysis. A purity as high as 90^{+15}_{-10} % is achieved with tight feed-down enhanced cuts in transverse momentum region $5 < p_T < 8$ GeV/c. The results of this study show that applying feed-down optimised topological selections is a viable method for selecting samples of feed-down D^{*+} with high purity.

Contents

1 Introduction

It is predicted that the early universe, a few microseconds after the Big Bang, was in a state with temperatures and densities so high that quarks and gluons were deconfined. This state in which the quarks and gluons are free to move, is called a quark-gluon plasma (QGP). As the universe expanded, the temperature and density dropped and the quarks and gluons would "freeze out", creating hadrons. Nowadays quark-gluon plasmas (QGP) can be studied by colliding heavy ions, for example in the *A Large Ion Collider Experiment* (ALICE) at the *Large Hadron Collider* (LHC). In these heavy-ion collisions hundreds of nucleons smash together creating a very dense and hot state of matter, a quark-gluon plasma. This quark-gluon plasma exists only for a moment and can not be studied directly. However particles produced during the collision interact with the plasma, and by detecting the particles leaving the collision properties of the QGP can be studied. Mesons with heavy quarks are excellent probes for studying the QGP. This is because the heavy quarks are formed during the early stages of the collision and consequently experience the QGP. D mesons are an example of these heavy-flavoured mesons, they consist of a charm quark/antiquark and an up, down or strange antiquark/quark. During the collision D mesons can be formed either directly from a charm quark, called prompt, or from B meson decays, called feed-down. A B meson is produced from a beauty (anti)quark and these beauty quarks have more than 3 times the mass of a charm quark. This mass difference of the charm and beauty quark may result in different interaction with the QGP. The more massive beauty quark is expected to loose less energy when traversing the QGP, due to the dead cone effect. Having a pure sample of feed-down D mesons would allow for accessing the beauty quark and consequently using these beauty quarks to probe the QGP. This would allow for experimental research of the mass effect on the energy loss in quark gluon plasma. Because of this it is important to be able to distinguish prompt and feed-down D mesons from each other and from the background. The ALICE detector can not detect D mesons directly, because they decay before reaching the detectors. However the D meson decay products can be detected. Compared to the prompt mesons, the feed-down mesons are on average more displaced from the collision point and as a result their decay topology will be different. Topological selections could allow for distinguishing feed-down from prompt D mesons by exploiting this difference in decay topology.

The study presented in this thesis is focused on finding selection values which increase the selection of feed-down D^{*+} mesons. These feed-down enhanced cuts are determined by comparing LHC data from Pb-Pb collisions at $\sqrt{s_{NN}} = 5.02$ TeV (centrality class 10-30%) with the corresponding Monte Carlo simulation. Four topological variables are studied and as a result two sets of cuts are chosen. Mass spectra are used to check the D^{*+} signal after applying the feed-down enhanced cuts. Additionally the efficiency and prompt fraction are presented.

The next sections of this thesis are structured as follows. Background information about the Standard Model, quark-gluon plasma, ALICE detector, D^{*+} meson and topological selection variables is presented in Section 2 *Background*. In Section 3 *Method* the methodology of this study is described, including what data is used and how it is processed. The main results of this research are presented in Section 4 *Results* and discussed in Section 5 *Conclusion and*

discussion. An outlook to future studies is written in Section 6 *Outlook*.

2 Background

In this section the necessary background information for this study is presented. This includes a very brief overview of the Standard Model, quantum chromodynamics and the state of matter called quark-gluon plasma. Additionally information will be given about the Large Hadron Collider and one of its detectors, ALICE. The production and decay of the D^{*+} meson are also explained in this section. Finally information is given about the topological selection variables used to select D^{*+} mesons.

2.1 Standard Model

There are four fundamental forces in the universe: the electromagnetic, weak, strong and gravitational force. Three of these forces, the electromagnetic, weak and strong interactions, are described by a theory called the Standard Model. Besides these forces the Standard Model also includes all known elementary particles. These elementary particles are divided in two groups, fermions and bosons. Fermions are characterised by half-integer spin and respect the Pauli exclusion principle, while bosons have integer spin. These groups are in turn divided into subgroups. Fermions can be divided in quarks and leptons, and bosons are divided in gauge and scalar bosons. An overview of the elementary particles in the Standard Model is given in Figure 1

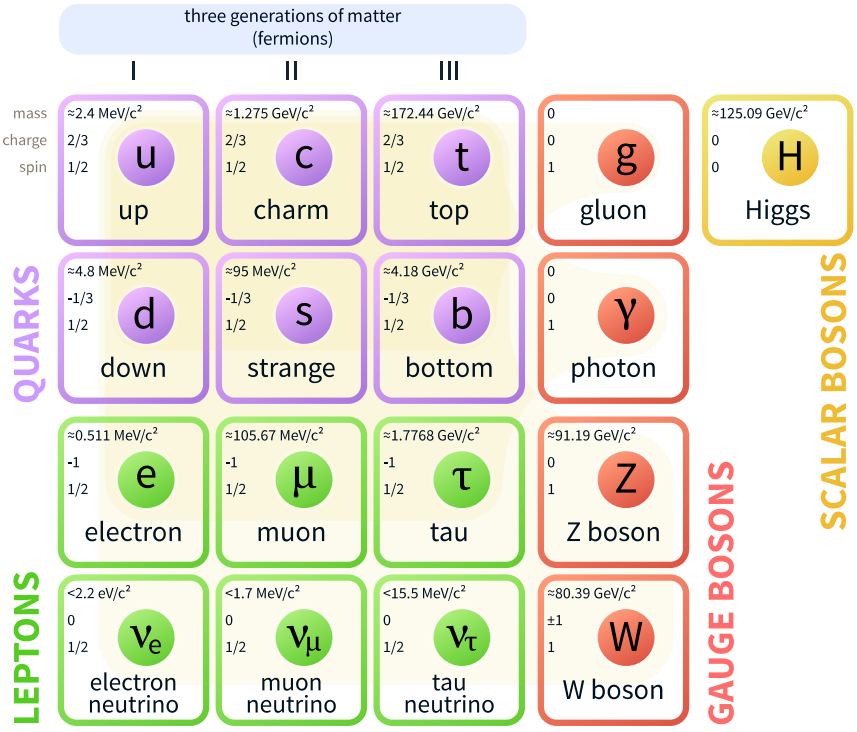

Figure 1: Overview of the Standard Model of elementary particles [1].

Fermions are divided into quarks and leptons based on the properties of the particle. Quarks carry colour charge and participate in all four fundamental interactions, while leptons do not have colour charge and only experience three of the fundamental forces (electromagnetic, weak and gravitational). There are six quarks (up, down, charm, strange, top/truth, bottom/beauty), and six leptons (electron, electron neutrino, muon, muon neutrino, tau, tau neutrino). Additionally all these quarks and leptons have corresponding antiquarks and antileptons. The quarks and leptons are separated in three generations of two particles (indicated as I, II, III in Figure 1), with the particles in the higher generations having more mass. Quarks make up baryons, baryons consisting of three quarks are called hadrons, and baryons with two quarks are called mesons. An example of an hadron is a proton containing two up quarks and one down quark (uud). The particle of interest in this study, D^{*+}, is a meson consisting of a charm and an antidown quark ($c\bar{d}$).

The gauge bosons mediate 3 of the four fundamental forces. The massless and neutral gluon mediates the strong interaction. The also massless and chargeless photon is the force carrier of the electromagnetic interaction. The weak interaction is mediated by the Z and W bosons. There are two W bosons, the W^+ and its antiparticle W^-, these are charged particles, while the Z is neutral. The in 2012 discovered Higgs boson is categorized in the other group of bosons, called scalar bosons. The Higgs boson, is responsible for the Higgs field and is used to explain why some fundamental particles have mass.

2.2 Quantum chromodynamics

Quantum chromodynamics describes the theory of the strong interaction, one of the four fundamental forces. Chromo from the Greek $\chi\rho\omega\mu\alpha$, meaning colour, refers to the theory of colour charge. Colour is a property quarks and gluons possess and is seen as the QCD analogue of electric charge in quantum electrodynamics (QED). In QED photons mediate the electromagnetic force between electrically charged particles, analogous QCD has gluons mediating the strong force between coloured particles. Here the theories of QED and QCD differ: photons are electrically neutral, while gluons do carry colour charge. Because gluons have colour charge they not only interact with quarks but also with other gluons. Both QED and QCD are described with a coupling constant. The QCD analogue of the QED fine structure constant is

$$\alpha_s = \frac{12\pi}{(11n - 2f)\ln\frac{|Q^2|}{\Lambda^2_{QCD}}},$$

where n is the number of colours available for each quark (3 colours), f is the number of quark flavours (6 flavours), Q is the transfer of exchanged four momentum and the QCD scale, Λ_{QCD}, is a constant [2]. For short distances the coupling constant α_s is very small, meaning quarks can move like free particles within small distances, i.e. inside of hadrons. This is known as asymptotic freedom. On the other hand α_s becomes very large for large distances. Lattice QCD has been developed to numerically solve the problems for large α_s. The results of these calculations predict that a phase transition from hadronic matter to a state of deconfined quarks and gluons can occur at very high temperatures and/or pressures. This state of matter is called the quark-gluon plasma (QGP). Figure 2 shows the predicted phase transition between hadronic matter and QGP in a phase diagram.

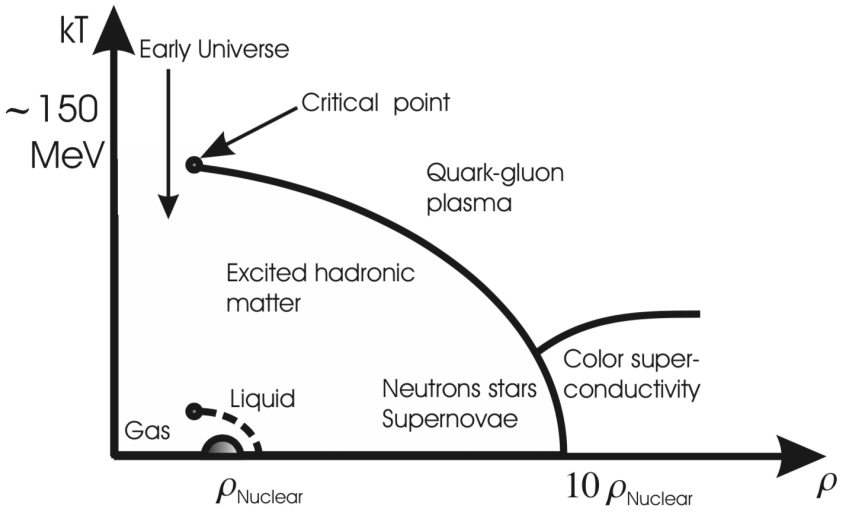

Figure 2: Phase diagram for hadronic matter, indicating the quark-gluon plasma state at very high temperature and/or pressure [3].

2.3 Quark-gluon plasma

The theory of quantum chromodynamics predicts a state called quark-gluon plasma (QGP) at very high temperatures and/or densities. In this state quarks and gluons are no longer confined to hadrons and are able to move through the plasma like free particles. It is predicted that shortly after the Big Bang the universe was filled with QGP for a couple of microseconds. To learn more about the early universe the quark-gluon plasma state needs to be studied.

Nowadays quark-gluon plasmas can be created for very short moments by colliding heavy ions. QGP are studied in for example the *A Large Ion Collider Experiment* (ALICE) at the *Large Hadron Collider* (LHC). In these heavy-ion collisions hundreds of nucleons smash together creating a very dense and hot state of matter in which the nucleons "melt" together, a quark-gluon plasma. The evolution of the system created in these collision consists of several stages, Figure 3 shows a spacetime diagram of this evolution.

- **Collision** The heavy-ion collisions are characterised by the center-of-mass energy $\sqrt{s_{NN}}$ (energy per nucleon-nucleon pair) and the centrality of the collision. The centrality class is related to the impact parameter b, which is the distance (in the transverse plane) between the centres of the two colliding nuclei.

- **Pre-equilibrium** In this stage particles are produced in the collision region. The exact mechanisms for this are not yet completely understood.

- **QGP** The system becomes in local thermal equilibrium and expands due to the difference in pressure between its surroundings. The viscosity of the QGP seems to be extremely low, allowing the expansion to be described as a perfect fluid.

- **Hadronisation** As the QGP expands, its temperature and density drop. This results in a phase transition to a state were the quarks and gluons are again confined in hadrons. The QGP can no longer exist and the system hadronises.

- **Freeze-out** The hot hadronic gas expands and cools down further. The decrease of temperature and density will results in less and less interactions between the hadrons.

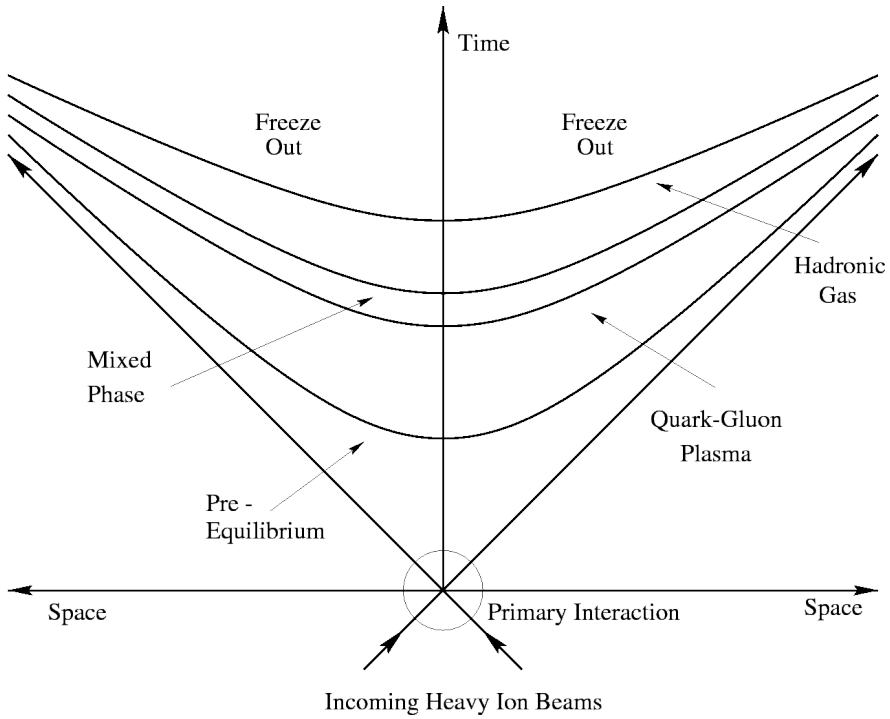

Figure 3: Spacetime diagram of the evolution of a heavy-ion collision. The collision evolves over time: collision, pre-equilibrium, QGP, hadronisation and freeze-out [4].

The QGP resulting from heavy-ion collisions is very short lived and cannot be measured directly. To study properties of the QGP we need to look at particles flying away from the collision, called probes. Since the strong force plays a large roll in the QGP, particles which experience this force should be used as probes. Quarks independently cannot be measured, but hadrons can be detected. In particular hadrons containing heavy quarks, such as B or D mesons are interesting because of the following. Heavy quarks are produced in the early stages (pre-equilibrium) of the collision, before the QGP is formed, and decay afterwards. While traveling through the QGP medium these quarks can lose energy via elastic scatterings (collisions with partons of the medium) and gluon radiation (gluonsstrahlung). This second process is similar to electrons in an electromagnetic field losing energy by radiating photons (Bremsstrahlung). The gluon radiation is predicted to be suppressed for emission angles $\theta \leq \frac{m_q}{E_q}$, with m_q and E_q the mass and energy of the quark respectively. This is called the dead cone effect and because of this effect the heavier quarks will radiate away less energy in the quark gluon plasma.

2.4 Research at CERN

CERN, abbreviation of *Conseil Europen pour la Recherche Nuclaire* (french for European Council for Nuclear Research), is an organisation where physicists and engineers study the fundamental structure of the universe. CERN is based near the Swiss-French border near Geneva and was established in 1954 by 12 European countries. At the moment CERN has 22 member states. The main focus of CERN is researching high-energy physics using particle

accelerators. CERN has a large complex of accelerators and detectors, see Figure 4 for a schematic overview. These accelerators deliver particles to experiments or first to another accelerator to increase the energies even further before performing the experiment. Outside of physics, research at CERN has also had a huge impact on the world because it is where the World Wide Web was invented. In the next sections the *Large Hadron Collider* (LHC) and one of its experiments, ALICE will be discussed.

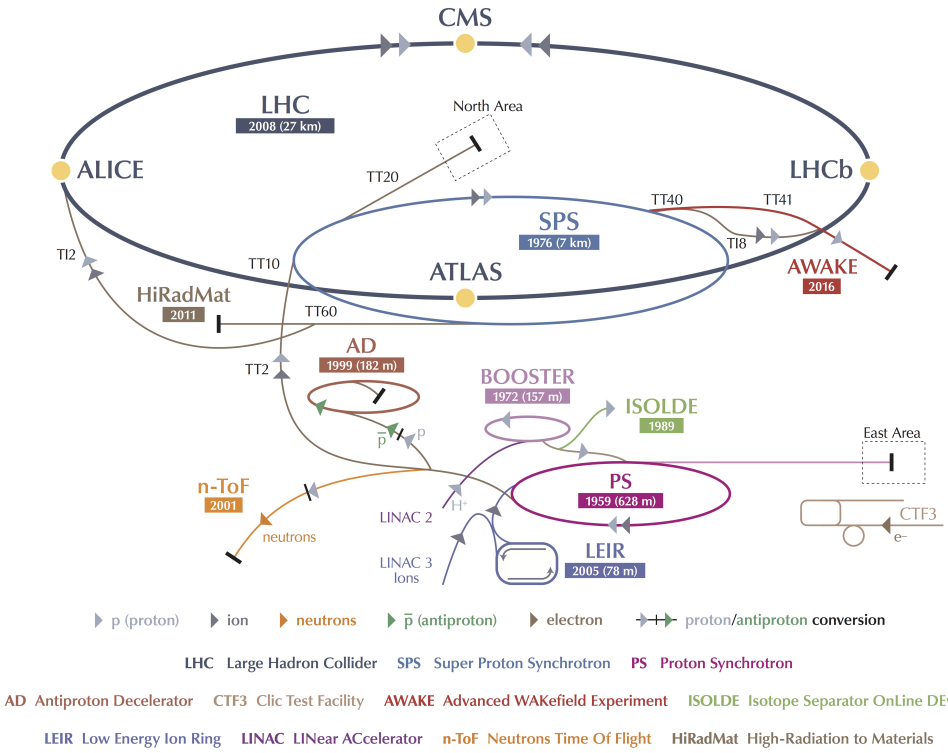

Figure 4: Schematic overview of CERN's accelerator complex. LHC is the largest ring (dark grey) in a complex chain of particle accelerators. Smaller accelerators are used sequentially to increase the particles energies and are also used for a selection of smaller experiments [5].

2.4.1 The Large Hadron Collider

The Large Hadron Collider is one of the accelerators located at CERN. It is a circular particle accelerator (synchrotron) 27 km in circumference and is located between 50 to 175 meters underground [6]. Presently the LHC is the largest and most powerful particle accelerator in the world, but even larger accelerators have been proposed by physicists: Future Circular Collide (FCC) and International Linear Collider (ILC).

LHC began operating in 2009 and is still used in the present. During this time mainly lead-lead (Pb-Pb), proton-proton (p-p), and proton-lead (p-Pb) collisions were studied. These particles are accelerated in smaller accelerators before being injected into the LHC. The LHC contains two separate ultrahigh vacuum beam pipes, which allow particle beams to travel in opposing directions. In these beamlines the particles are accelerated using radiofrequency

cavities and along the way the path of the particles is bend using dipole magnets, otherwise the beam of particles would travel in a straight line and collide with the inside of the beam pipe. To keep the beam of particles from diverging pairs of quadrupole magnets are used, these act likes lenses and focus the beam. By alternating these radiofrequency cavities, deflection magnets and focusing magnets the beam of particles can be accelerated while keeping it focused and in the center of the circular beam pipe. Finally the two opposing beams can collide at one of the four beam intersections. The center-of-mass energies reached in these collisions are up to $\sqrt{s_{NN}} = 5.02$ TeV (NN: per nucleon-nucleon pair) for Pb-Pb and $\sqrt{s} = 14$ TeV for p-p collisions. To study these collisions the LHC has four main detectors [7]:

- ***A Toroidal LHC ApparatuS* (ATLAS)** A general-purpose detector for studying a broad range of physics, including the Standard Model, extra dimensions and dark matter.
- ***Compact Muon Solenoid* (CMS)** This is another general-purpose detector with similar goals as ATLAS, but a different experimental design.
- ***A Large Ion Collider Experiment* (ALICE)** ALICE studies the physics of strongly interacting matter, including quark-gluon plasma.
- ***Large Hadron Collider beauty* (LHCb)** In this experiment differences between matter and antimatter are investigated by studying the beauty quark.

Additionally three specialised detectors are used to study the collisions in the LHC: *TOTal Elastic and diffractive cross section Measurement* (TOTEM), *Monopole and Exotics Detector At the LHC* (MoEDAL) and *Large Hadron Collider forward* (LHCf). In the next section the detector of interest for this study, ALICE, is handled in more detail.

2.4.2 The ALICE detector

One of the four main detectors at LHC is the *A Large Ion Collider Experiment* (ALICE). ALICE is 26 m long, 16 m high, 16 m wide weighs more than $10,000,000$ kilograms and is located in a cavern 56 meters underground [8]. To study the ultra-relativistic heavy-ion collisions, specifically lead-lead collisions, ALICE uses a complex system of sub-detectors. Besides Pb-Pb collisions ALICE also studies proton-lead and proton-proton collisions, these are useful for reference. Figure 5 shows a schematic illustration of the ALICE detector. Inside the large red solenoid magnet the following sub-detectors are located (from inside to outside): *Inner Tracking System* (ITS), *Time Projection Chamber* (TPC), *Transition Radiation Detector* (TRD), *Time Of Flight* (TOF) detector, *High Momentum Particle IDentification* (HMPID) detector, *PHOton Spectrometer* (PHOS) and *ElectroMagnetic Calorimeter* (EMCal). Inside the large magnet the path of charged particles is bend by a magnetic field of $B = 0.5$ T parallel to the beam direction (denoted as z-direction).
ALICE also has the following detectors, which are used for triggering and determining properties about the initial conditions of the collision (such as time of collision, number of particles involved): FMD, T0, V0, PMD and ZDC.

The ITS, TPC and TOF sub-detectors are very important for the reconstruction of D^{*+} mesons, therefore these sub-detectors will be discussed in more detail in the following sub-sections. For a more comprehensive review of ALICE and its sub-detectors please refer to [9].

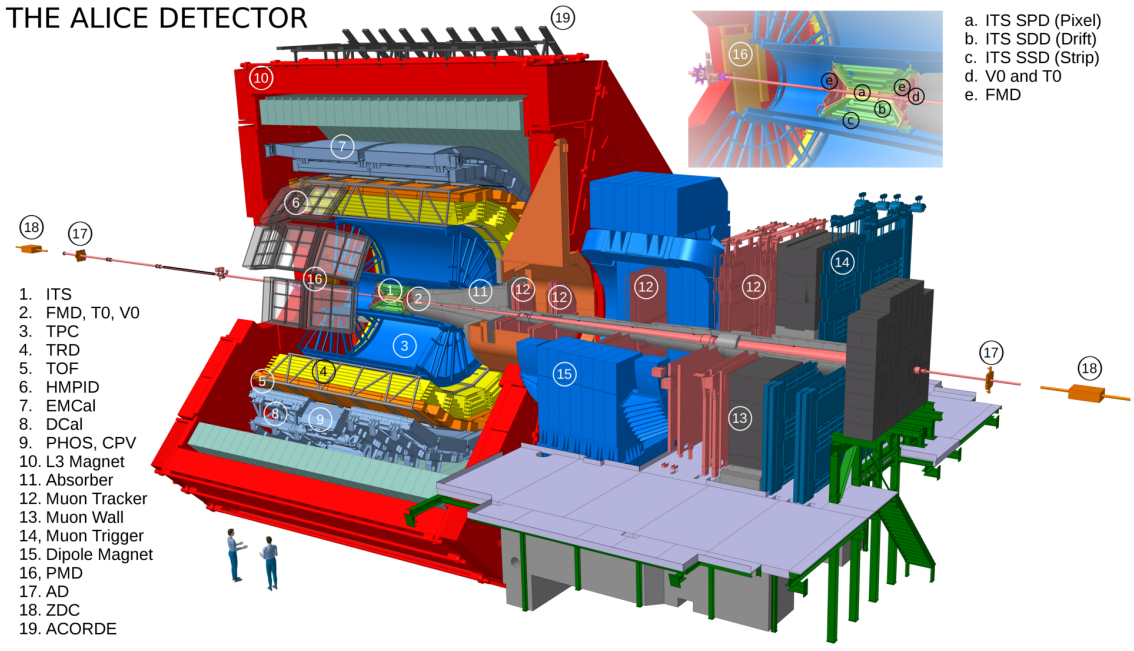

Figure 5: Schematic of the ALICE detector, indicating the various sub-detectors [10].

Inner Tracking System The first sub-detector particles produced in the collision will reach is the Inner Tracking System (ITS). The main purpose of this detector is to locate the vertex where the detected particles originate from. Some particles will originate from the primary vertex (point of collision), while other particles will come from the decay of other particles (secondary vertices) located away from the primary vertex. Figure 6 shows the structure of the ITS, it consists of six cylindrical silicon detector layers (from inside out): two *Silicon Pixel Detectors* (SPD), two *Silicon Drift Detectors* (SDD) and two *Silicon Strip Detectors* (SSD). These types of silicon sensors differ in resolution in both the beam direction (z-axis) and in the transverse plane (xy-plane).

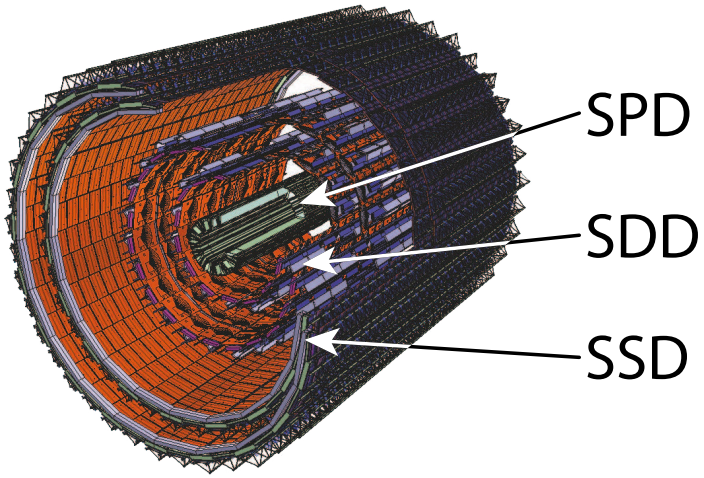

Figure 6: Schematic of the ALICE's *Inner Tracking System* (ITS). ITS consists of layers of *Silicon Pixel Detectors* (SPD), *Silicon Drift Detectors* (SDD) and *Silicon Strip Detectors* (SSD) [11].

Time Projection Chamber The main particle tracking device of ALICE is the *Time Projection Chamber* (TPC), located in ALICE's central barrel. In Figure 7 a schematic of the TPC is shown. This $90m^3$ chamber is filled with a gas mixture of mainly Ne gas and a small percentage of CO_2 and N_2. Charged particles entering the chamber can ionise the gas particles, leaving a trail of ionised gas particles. Consequently the freed electrons will move in an electric field to the wire chambers located at the ends of the cylindrical chamber. By detecting the arrival of the electrons on the wire planes, the trajectories of the charged particles can be reconstructed.

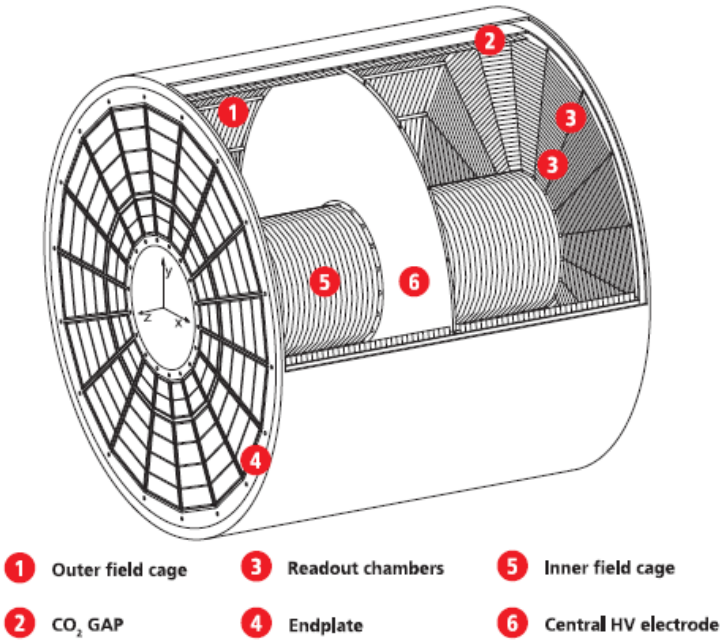

Figure 7: Schematic of the ALICE's *Time Projection Chamber* (TPC). The TPC is filled with a $Ne/CO_2/N_2$ gas mixture. A charged particle travelling through the gas can free electrons from the gas molecules. The detection of these electrons allows for the reconstruction of the charged particle's trajectory [12].

Using the reconstructed track the TPC is able to additionally measure the particle's momentum and specific energy loss dE/dx (due to ionisation of the gas). The energy loss as a function of momentum can be used to identify particles, see Figure 8. This allows the TPC to be used for particle identification.

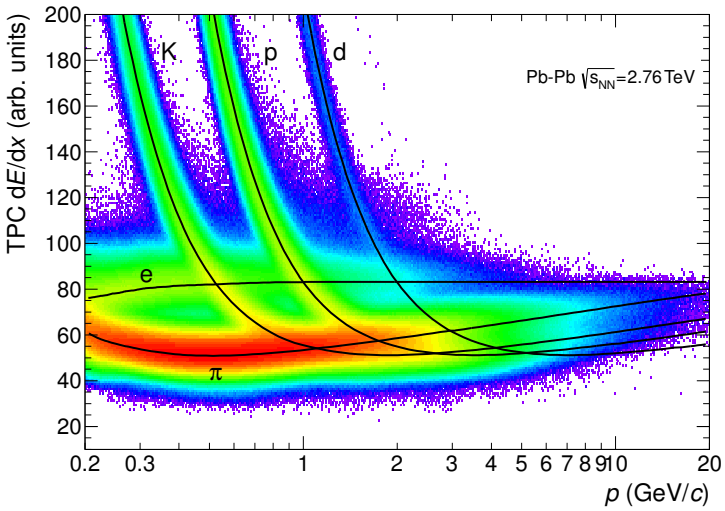

Figure 8: Specific energy loss dE/dx against particle momentum p. Data from the TPC detector of Pb-Pb collisions at $\sqrt{s_{NN}} = 2.76$ TeV. The lines indicate the characteristics of a number of different particles [13].

Time Of Flight detector The Time of Flight detector is located around the TRD, and its main use is particle identification. The TOF consists of hundreds of Multigap Resistive Plate Chambers (MRPC) which cover an area of about 160 m^2 [14]. An MRPC consists of a stack of resistive glass plates, a high voltage is applied to the outer surfaces of this stack. Charged particles ionise the gas in the chamber and this ionisation is amplified by the electric field, creating an electron avalanche. The resistive plates stop these avalanches, but they are transparent to the electron induced signal on the pickup electrodes. Figure 7 shows an illustration of a MRPC. The time measurement with the TOF, in combination with information from tracking detectors (momentum and track length) can be used to calculate the particle mass. Figure 8 shows how data from the TOF detector in combination with the particle momenta can be used to identify particles.

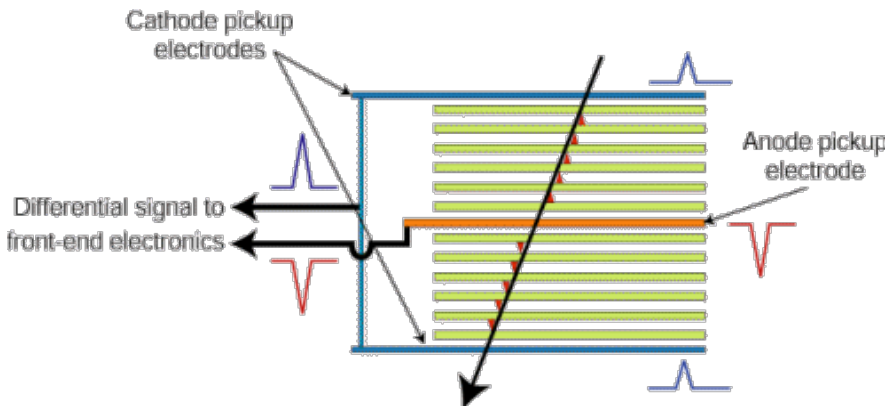

Figure 9: Illustration of a Multigap Resistive Plate Chamber (MRPC) used in ALICE's Time Of Flight (TOF) sub-detector. An MRPC consists of a stack of resistive glass plates. Charged particles ionise the gas in the chamber, resulting in electron avalanches. The resistive plates stop these avalanches, but allow the electron induced signal to be detected by the pickup electrodes [14].

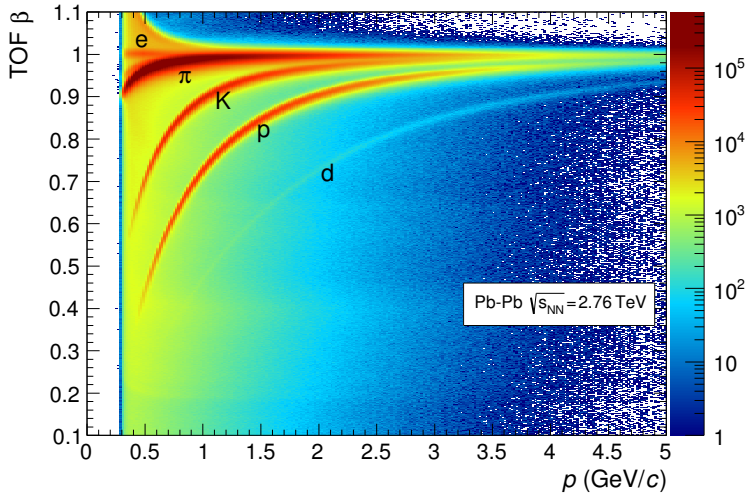

Figure 10: Measurement of the TOF detector, $\beta = v/c$, as a function of momentum for particles detected by TOF in Pb-Pb collisions at $\sqrt{s_{NN}} = 2.76$ TeV [13].

2.5 Production and decay of D^{*+} meson

The particle of interest in this study, D^{*+} mesons, are excited $c\bar{d}$ states and can be formed in heavy-ion collisions by two distinct ways. Either directly from charm quarks (called prompt), or indirectly from beauty quarks (called feed-down):

$$\begin{aligned} &\text{Prompt:} && c \to D^{*+} + \dots \\ &\text{Feed-down:} && b \to B \to D^{*+} + \dots, \end{aligned}$$

here B is a B meson containing a beauty quark/antiquark and an up, down, stange or charm antiquark/quark. There are multiple ways in which a charm or beauty quark can decay into

a D^{*+}, but in this study these processes will not be looked into, hence the "..." indicating the presence of additional decay particles. The mean life of a B meson is 1.566×10^{-12} s [15], this is orders of magnitude larger than the mean life of c quarks. The result of this is that feed-down D^{*+} will be produced further away from the primary vertex (point of collision) by about 470 μm (this is an approximation since the velocity of the B meson is less than the speed of light and not necessarily in a straight line). This is a useful distinguishing factor between prompt and feed-down D^{*+} and is of importance for the study presented in this thesis. In Section 2.6 *Topological variables* this difference will be used when discussing topological selection variables.

D^{*+} mesons decay before reaching the detectors in ALICE, but they can be detected indirectly by looking at the particles it decays into. In this study the reconstruction of D^{*+} mesons is done using the hadronic decay channel $D^{*+} \to D^0\ \pi_s^+ \to K^-\ \pi^+\ \pi_s^+$, here π_s^+ describes a pion with low momentum (soft pion). A sketch of this decay channel is shown in Figure 11. The branching ratios for these decays are [15]

$D^{*+} \to D^0\ \pi_s^+$	strong decay	$BR = (67.7 \pm 0.5)\%$
$D^0 \to K^-\ \pi^+$	weak decay	$BR = (3.89 \pm 0.04)\%$,

resulting in a branching ratio of $2.63 \pm 0.03\%$ for this decay channel. This means that on average about 2.63% of the D^{*+} produced in the heavy-ion collisions will decay following this decay channel.

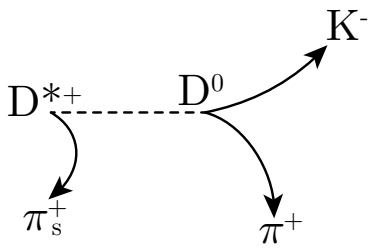

Figure 11: Sketch of the used D^{*+} decay channel: $D^{*+} \to D^0\ \pi_s^+ \to K^-\ \pi^+\ \pi_s^+$. The trajectories of the charged particles (kaon and pion) are bend by magnetic field in the detector.

2.6 Topological variables

In this study D^{*+} mesons from the decay channel $D^{*+} \to D^0\ \pi_s^+ \to K^-\ \pi^+\ \pi_s^+$ (Section 2.5), are reconstructed by the detection of the 3 particles: π_s^+, π^+ and K^-. By making combinations of 3 tracks corresponding to these 3 particles, one could expect to be able to reconstruct D^{*+} mesons. However, because of the relative scarcity of D^{*+} mesons and the thousands of possible tracks, this will result in the selection of mostly combinatorial background. The real D^{*+} will be indistinguishable from the background. For this reason selections based on the topology of the decay are applied. Choosing the selection values is a delicate procedure, they need to be tight enough to cut away as much background as possible, while still selecting the

desired real D^{*+}.

For the analysis of D^{*+} meson selections are made using the following topological properties:

- ΔM_{D^0}: invariant mass D^0
- DCA: distance of closest approach between K^- and π^+
- $\cos(\theta^*)$: cosine of angle between reconstructed D^0 and K^-
- $p_T(K)$ / $p_T(\pi)$ / $p_T(\pi_s)$: transverse momentum of the K^-, π^+ and π_s^+
- $d_{0,K}$ / $d_{0,\pi}$: impact parameter K^- and π^+
- $d_{0,K} \times d_{0.\pi}$: product of the impact parameters of K^- and π^+
- $\cos(\theta_{point})$ / $\cos(\theta_{point})_{XY}$: cosine of pointing angle (xy)
- Norm L_{XY}: Normalised decay length xy
- invariant mass half width of D^*
- half width of ($M_{K\pi\pi}$-M_{D^0})
- angle between the π_s^+ and decay plane of the D^0.

In this study four of these topological selection variables are studied in detail: $d_{0,K}$, $d_{0,\pi}$, $\cos(\theta_{point})$ and Norm L_{XY}. These selection variables are used because the difference in D^{*+} formation distance of prompt and feed-down D^{*+} (caused by the relatively long decay length of the B meson, mentioned in Section 2.5) is expected to result in different distributions for prompt and feed-down. In the following subsections these four topological variables will be treated in detail.

2.6.1 Impact parameter kaon and pion

The impact parameter kaon ($d_{0,K}$) and pion ($d_{0,\pi}$) is a selection variable based on the D^0 decay products. It is measured as the distance of closest approach of the particle track to the primary vertex. A sketch of the impact parameters is shown in Figure 12. D^0 mesons coming from feed-down D^{*+} will on average decay further away from the primary vertex than D^0 coming from prompt D^{*+}. This will result in larger impact parameters for the feed-down process and consequently the kaon and pion impact parameter distribution for the feed-down process is expected to be shifted to larger values relative to the prompt distribution.

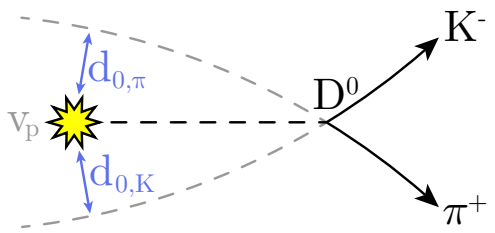

Figure 12: Illustration showing the impact parameter (closest approach to the primary vertex v_p) of the kaon ($d_{0,K}$) and pion ($d_{0,\pi}$) track from D^0 decay.

2.6.2 Cosine pointing angle

The pointing angle (θ_{point}) is measured as the angle between the direction of the D^0 reconstructed momentum (p_{D^0}) and the line connecting the primary and secondary vertex, see Figure 13 for an illustration. This angle will be close to 0 for D^0 coming from real prompt and feed-down D^{*+}. Therefore the distribution of the cosine pointing angle is expected to peak around 1.

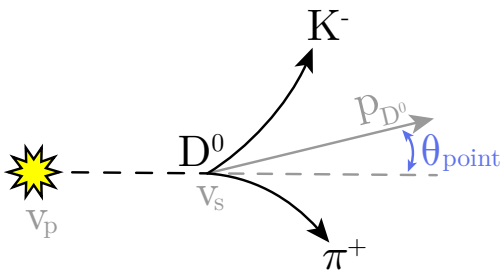

Figure 13: Illustration of the pointing angle (θ_{point}) between the direction of the reconstructed D^0 momentum (p_{D^0}) and the line from the primary (v_p) to secondary vertex (v_s). The cosine of this angle ($\cos(\theta_{point})$) is used as selection variable.

2.6.3 Normalised decay length xy

The decay length (L) is defined as the distance between the primary vertex and the reconstructed secondary vertex. This is an approximation of the real decay length since the trajectory of the D^{*+} is curved by the detectors magnetic field. The difference is however small because of the short mean life of the D^{*+}. The decay length is very useful for distinguishing real D^{*+} from background candidates, because on average L is larger for real D^{*+} than background candidates. By projecting the decay length in the transverse plane of the beam (xy-plane), the decay length xy (L_{XY}) is obtained. This is done because the detector has a higher resolution in the xy-plane than the z-direction. To increase the difference between signal and background candidates the decay length xy is divided by its uncertainty, this result is called the normalised decay length xy (Norm L_{XY}). Figure 14 shows an illustration of the decay length xy.

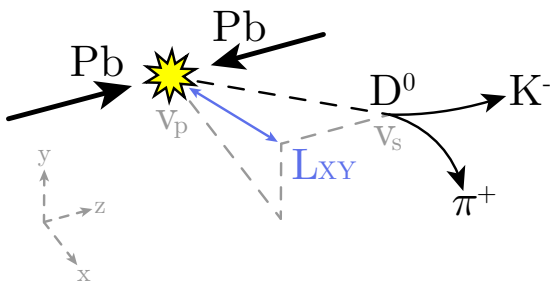

Figure 14: Illustration of the decay length in the xy-plane (L_{XY}). The normalised decay length xy (Norm L_{XY}) is defined as L_{XY} divided by its uncertainty.

3 Method

3.1 Overview

This study is focused on determining selection values for four different topological variables, which increase the selection of feed-down D^{*+} mesons. The four topological variables of interest, as mentioned in Section 2.6, are: $d_{0,K}$, $d_{0,\pi}$, $\cos(\theta_{point})$ and Norm L_{XY}. Selection values (also called cut values) can be explained as follows: select D^{*+} candidates for which the topological value is above/below the selection value, while cutting away the candidates below/above this value. So the selections actually consist of two parameters, the value (x) and whether to select above ($> x$) or below ($< x$) this value. In this study the selection values are determined for 13 D^{*+} transverse momenta (p_T D^{*+}) intervals, ranging from $1-50$ GeV/c. Different momenta regions are used because the number of feed-down and prompt D^{*+} mesons depends on the momenta of the D^{*+}. Real Pb-Pb collision data and Monte Carlo (MC) simulations from ALICE are used for this study. By comparing the real and simulated data the feed-down enhanced cuts are determined, for each of the four selection variables, using the following process.

- First, the topological variable distributions are extracted from the real data set and Monte Carlo simulation. Because the Monte Carlo data set is simulated, it is known exactly which of the D^{*+} are prompt and which are feed-down. So the MC topological variable distribution is separated in two: MC prompt and MC feed-down. In comparison to prompt, the feed-down D^{*+} are on average displaced further away from the primary vertex. As a result the topological variable distributions for MC feed-down are expected to have a different shape compared to MC prompt. The 3 distributions, data, MC prompt and MC feed-down, for each of the 13 p_T D^{*+} regions, are normalised and fitted.

- The fitted distributions are used to calculate two ratios: $\frac{\text{MC prompt}}{\text{data}}$ and $\frac{\text{MC feed-down}}{\text{data}}$. By comparing these ratios, the regions that increase the selection of feed-down D^{*+} can be investigated and feed-down enhanced cuts can be determined for each p_T D^{*+} interval.

- For each p_T D^{*+} interval the number of entries within the selection regions, determined in the previous step, is calculated and divided by the total number of entries. This is

done for both MC prompt ($N^{\text{after cut}}_{\text{prompt}}/N_{\text{prompt}}$) and MC feed-down ($N^{\text{after cut}}_{\text{feed-down}}/N_{\text{feed-down}}$). These fractions give an estimation of the fraction of respectively prompt and feed-down D^{*+} selected after applying the cuts.

In this study two sets of these feed-down enhanced cuts are presented. A set of loose cuts and a set of tight cuts. The loose cuts are focused on increasing the feed-down D^{*+} contribution without cutting away too much of the D^{*+} candidates. While the tight cuts are chosen with high prompt rejection in mind. These tight cuts will cut away a large percentage of all D^{*+} candidates and will result in an increased feed-down contribution but also lower statistics compared to the loose cuts. A set of standard cuts is presented for comparison. These standard analysis cuts are optimised at obtaining a large signal-to-background ratio and consequently a large significance. The loose and tight feed-down enhanced cuts, as well as the standard analysis cuts, are individually applied to the real Pb-Pb data from ALICE. The results of applying these 3 different sets of cuts are analysed by comparing the invariant mass spectra, efficiency and prompt fraction.

Before presenting the results of this study in Section 4, the following subsections will give more information about the used programming environment, LHC data, Monte Carlo simulation and analysis methods.

3.2 ROOT framework

The ROOT programming framework is used in this study. ROOT is a modular scientific software framework developed by CERN and is mainly used for data acquisition, analysis and visualisation in particle physics [16]. Other uses of ROOT are in astronomy and data mining. ROOT development started in 1994 by René Brun and Fons Rademakers and is written object-oriented in C++. The ROOT distribution comes with a lot of example macros, which can be edited. Of course users can also create their own custom macros. The macros can be executed using an interpreter or by running the code after compiling.

AliRoot is a framework developed for the ALICE detector, it uses ROOT as foundation and adds features for analysis of real data from ALICE, event generation and detector simulation [17]. AliRoot comes bundled with a large selection of macros ready for use.

The Worldwide LHC Computing Grid (WLCG), often just called grid, is used for computation intensive analysis and simulation tasks. Supervisor S. Jaelani ran code on the grid for some of the analyses in this study.

Some of the important ROOT classes used during this study are: *TH1* for creating histograms and *TF1* for describing fit functions. AliRoot macros used in this study include: *makeTFile4CutsDStartoKpipi.C* for writing the cuts files, *FitMassSpectra.C* for creating and fitting invariant mass spectra, *HFPtSpectrumRaa.C* for calculating the prompt fraction and *DrawEfficiency.C* for calculating the efficiency. All these macros can be found in the *PWGHF/vertexingHF* directory.

3.3 Data and Monte Carlo simulation

In this study two data sets are used, one from real Pb-Pb collisions and the other from simulated collisions:

- **LHC15o** Data from ALICE of real Pb-Pb collision at $\sqrt{s_{NN}} = 5.02$ TeV, centrality class 10-30%. The run numbers are tabulated in Table 1 and number of events are approximately 23 million.
- **LHC16i2a** Monte Carlo simulation of Pb-Pb collisions in ALICE using the PYTHIA event generator (part of the AliRoot distribution). The number of events are approximately 5.5 million.

In the Monte Carlo simulations, properties (such as origin position, momentum, mother- and daughter-particles) can be looked up for every particle produced in the collision, even for particles which in real collisions would decay before reaching the detectors. This allows for the crucial distinction of prompt and feed-down D^{*+} mesons in the Monte Carlo simulation set. The Monte Carlo simulation is not only used to investigate the differences in topological variable distributions between prompt and feed-down D^{*+}, but also to analyse the quality of determined feed-down enhanced cuts (efficiency and prompt fraction).

Table 1: LHC15o run numbers of Pb-Pb collisions in 2015.

LHC pass	Run numbers
LHC15o_pass1	245683, 245692, 245702, 245705, 245829, 245831, 245833, 245923, 245949, 245952, 245954, 246001, 246003, 246012, 246036, 246037, 246042, 246048, 246049, 246052, 246053, 246087, 246089, 246113, 246115, 246148, 246151, 246152, 246153, 246178, 246180, 246181, 246182, 246185, 246217, 246222, 246225, 246271, 246272, 246275, 246276, 246424, 246431, 246434, 246487, 246488, 246493, 246495, 246750, 246751, 246757, 246758, 246759, 246760, 246763, 246765, 246766, 246804, 246805, 246807, 246808, 246809, 246810, 246844, 246845, 246846, 246847, 246851, 246928, 246945, 246948, 246982, 246984, 246989, 246991, 246994
LHC15o_pass1_pidfix	245145, 245146, 245148, 245151, 245152, 245231, 245232, 245233, 245259, 245343, 245345, 245346, 245347, 245349, 245353, 245396, 245397, 245401, 245407, 245409, 245410, 245411, 245439, 245441, 245446, 245450, 245452, 245453, 245454, 245496, 245497, 245501, 245504, 245505, 245507, 245535, 245540, 245542, 245543, 245544, 245545, 245554
LHC15o_pass3_lowIR_pidfix	244918, 244975, 244980, 244982, 244983, 245061, 245064, 245066, 245068, 246390, 246391, 246392

3.4 Analysis

The results of applying the determined feed-down enhanced cuts are compared with the standard analysis cuts by looking at the invariant mass spectra, efficiency and prompt fraction.

3.4.1 Invariant mass spectra

To identify particles the invariant mass property is often used:

$$M = \sqrt{E^2 - \|\overrightarrow{p}\|^2}.$$

The D^{*+} signal is analysed by looking at the difference between the invariant mass of D^{*+} and D^0,

$$\Delta M = M(D^{*+}) - M(D^0).$$

Since the D^{*+} and D^0 decay before reaching the detector, their invariant masses can not be measured directly. Instead their decay products (kaons and pions) are used to reconstruct the invariant masses,

$$M(D^{*+}) = M(K^-\pi^+\pi_s^+),$$
$$M(D^0) = M(K^-\pi^+).$$

The difference in D^0 and D^{*+} invariant mass is used because this way the uncertainties in the kaon and pion momenta cancel out, resulting in a better accuracy. The peak width is now basically only affected by the soft pion (π_s^+) momentum.

While the topological selections are aimed at selecting real feed-down D^{*+} candidates, a certain amount of prompt and background candidates will also pass the topological selections. All these selected D^{*+} mesons, real and background, will be added as entries to the invariant mass spectra. If the topological selections are good, the real D^{*+} signal will be visible as a significant peak above the background. This peak will be located slightly higher than the mass of a π^+, around 145MeV/c^2. The invariant mass difference (ΔM) distributions of D^{*+} candidates are fitted with a Gaussian function for the signal and a threshold function multiplied by an exponential for the background:

$$a\sqrt{\Delta M - m_\pi} \cdot e^{b(\Delta M - m_\pi)}.$$

Using these fits the number of entries is calculated for the signal (S, raw yield) and background (B) in a region of three sigma (3σ) around the Gaussian signal. The significance of the signal, defined as

$$signif. = \frac{S}{\sqrt{S+B}},$$

can be calculated with S and B.

3.4.2 Efficiency and prompt fraction

While the invariant mass spectra can be used to indicate if the applied topological selections are proficient at selecting real D^{*+} candidates, these spectra do not provide any information about the contribution of prompt and feed-down candidates. To analyse this aspect of the cuts, the efficiency and prompt fraction are used.

The efficiency is calculated using the Monte Carlo simulation and is defined as the number of D^{*+} selected after all the topological and PID selections, divided by the number of generated $\mathrm{D}^{*+} \to \mathrm{D}^0\ \pi_s^+ \to \mathrm{K}^-\ \pi^+\ \pi_s^+$ decays.

The prompt fraction, defined as [18]

$$\begin{aligned} f_{prompt} &= 1 - \frac{N_{\mathrm{raw}}^{D\ \text{feed-down}}}{N_{\mathrm{raw}}^{D}} \\ &= 1 - \langle T_{\mathrm{AA}} \rangle \cdot \Big(\frac{\mathrm{d}^2\sigma}{\mathrm{d}_{p_T}\mathrm{d}y} \Big)_{\text{feed-down}}^{\text{FONLL}} \cdot R_{\mathrm{AA}}^{\text{feed-down}} \cdot \frac{(\mathrm{Acc} \times \epsilon)_{\text{feed-down}} \cdot \Delta y \Delta p_T \cdot \mathrm{BR} \cdot N_{\mathrm{evt}}}{N_{\mathrm{raw}}^{D+\bar{D}}/2}, \end{aligned}$$

uses the raw yields to calculate the fraction of prompt D^{*+} selected. For the standard analysis this prompt fraction is close to one, meaning that the selected D^{*+} candidates are mostly prompt. For the feed-down enhanced cuts lower prompt fractions in comparison to the standard analysis are desired.

Related to the prompt fraction is the purity of the sample, which is defined as the number of feed-down D^{*+} divided by all (prompt and feed-down) D^{*+} mesons:

$$purity = \frac{N_{\text{feed-down}}^{\mathrm{D}^{*+}}}{N^{\mathrm{D}^{*+}}}.$$

4 Results

The main results of this study are presented in this section. First the process of choosing the feed-down enhanced cuts is reported for the four topological variables. Secondly the determined cut values are summarised in Section 4.5. In the final three subsections the invariant mass spectra, efficiencies and prompt fractions are reported.

4.1 Impact parameter kaon

The impact parameter kaon ($d_{0,K}$) distributions for data, MC prompt and MC feed-down are presented in Figure 15. These histograms are fitted using log-normal distributions. The impact parameter distributions for the feed-down D^{*+} mesons are broader (not as sharply peaked) and shifted to the right compared to the prompt distributions. This is because the feed-down D^{*+} momentum is not necessarily parallel to the momentum of the B hadron. As a result the impact parameters for kaon and pion coming from feed-down D^{*+} will be on

average slightly larger.

The ratios, $\frac{\text{MC prompt}}{\text{data}}$ and $\frac{\text{MC feed-down}}{\text{data}}$, of the $d_{0,K}$ distributions are shown in Figure 16. In each p_T interval the intersection of these ratios is located between $0.01-0.02$ cm. To the right of the intersection the feed-down/data ratio is dominant, while to the left the prompt/data ratio is larger. These intersections are chosen as the loose feed-down enhanced cut values: select D^{*+} candidates for which $d_{0,K}$ is larger than intersection, while cutting away the candidates with smaller $d_{0,K}$. Using this cut, the region where feed-down D^{*+} are relatively more abundant is selected.

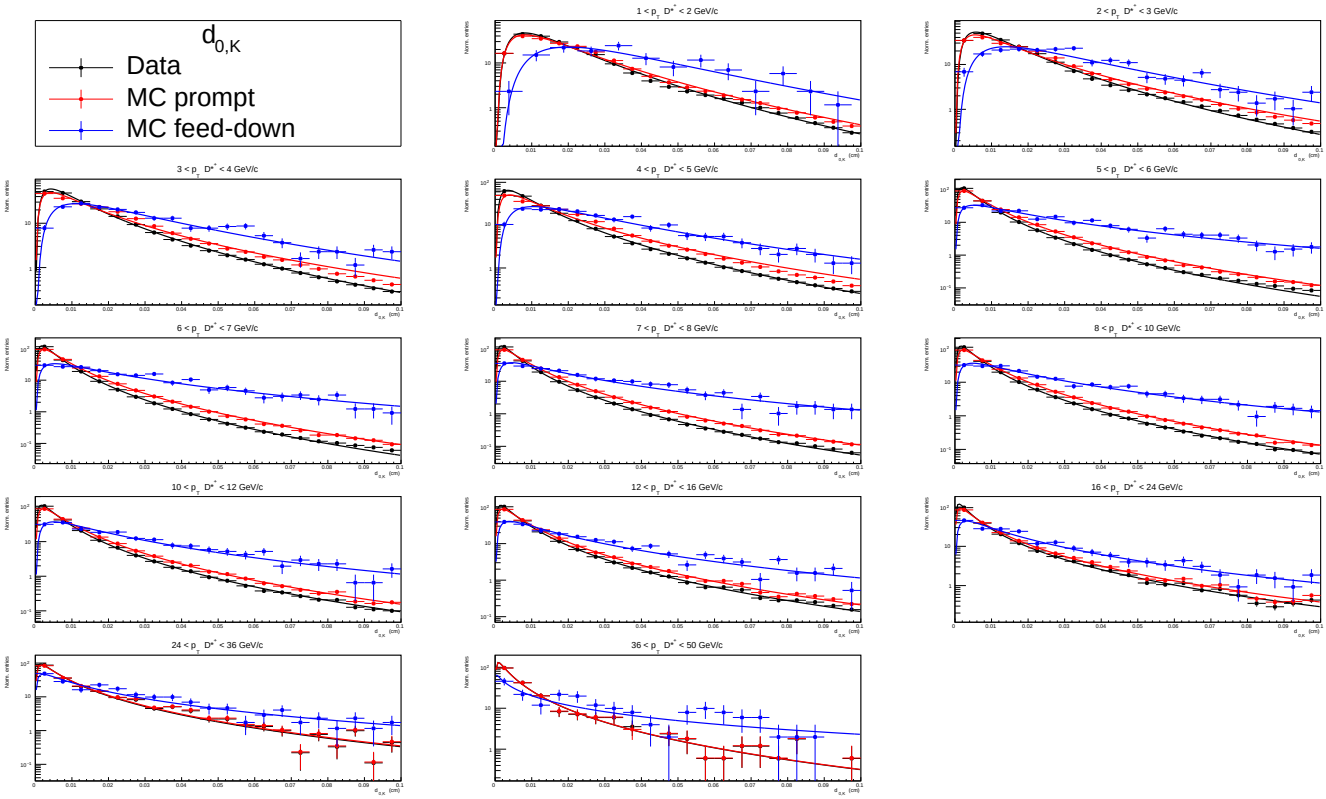

Figure 15: Normalised impact parameter kaon ($d_{0,K}$) distributions for data (black), MC prompt (red) and MC feed-down (blue), separated in 13 D^{*+} p_T intervals. Y-axis has logarithmic scale. Fitted with log-normal distribution. The MC feed-down distributions are broader (not as sharply peaked) and shifted to the right compared to the MC prompt distributions.

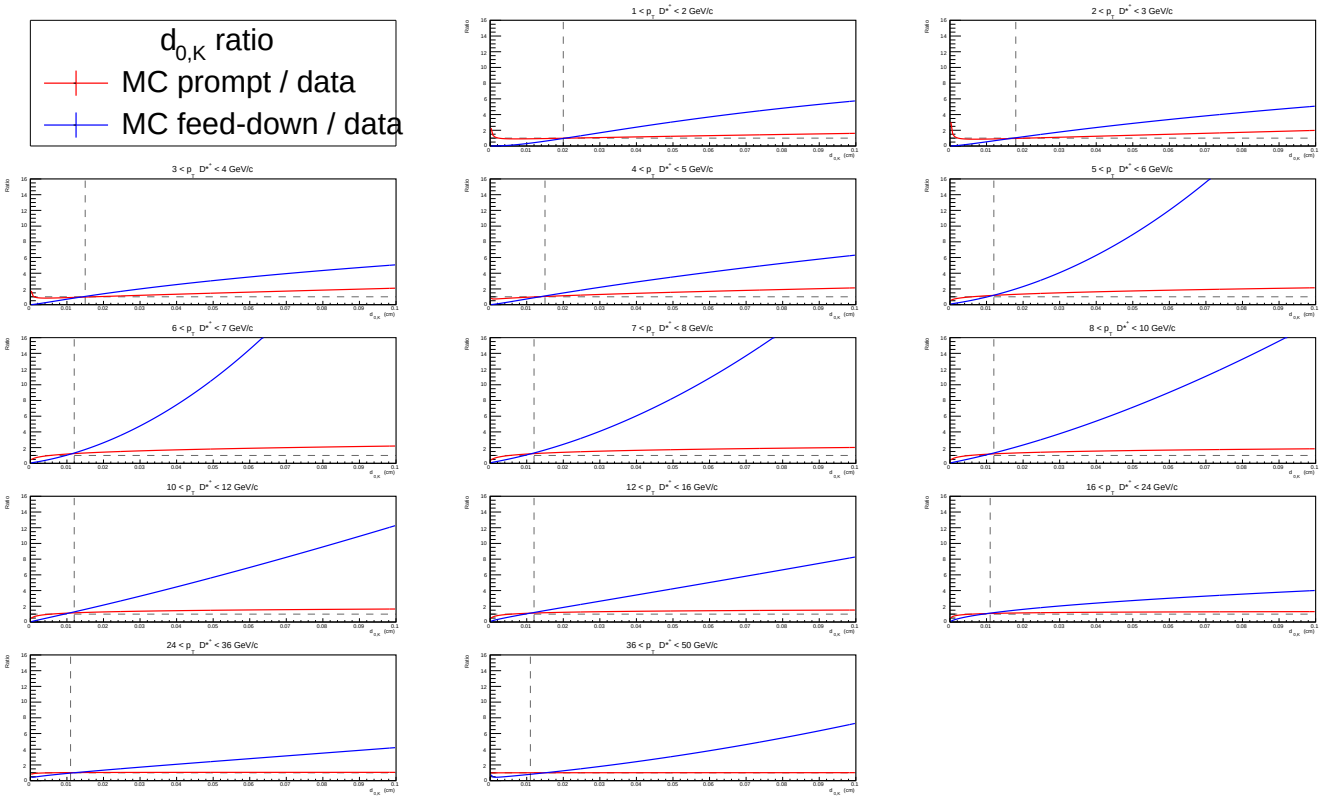

Figure 16: Ratios of the impact parameter kaon ($d_{0,K}$) fits: $\frac{\text{MC prompt}}{\text{data}}$ (red) and $\frac{\text{MC feed-down}}{\text{data}}$ (blue). Separated in 13 D^{*+} p_T intervals. The intersections are around $0.01 - 0.02$ cm and for larger $d_{0,K}$ the $\frac{\text{MC feed-down}}{\text{data}}$ ratio becomes dominant. These intersections of the ratios are used as value for the loose cuts and are indicated with a vertical dashed line.

Using the Monte Carlo distributions the fraction of prompt ($N_{\text{prompt}}^{\text{after } d_{0,K} \text{ cut}}/N_{\text{prompt}}$) and fraction of feed-down ($N_{\text{feed-down}}^{\text{after } d_{0,K} \text{ cut}}/N_{\text{feed-down}}$) selected using these cuts is estimated for each p_T interval. The loose cuts select between $60 - 75\%$ of all feed-down entries and between $25 - 45\%$ of the original prompt, as seen in the left panel of Figure 17. A step in the estimated fraction of prompt is seen between $4 - 5$ GeV/c. This is caused by pre-selections. As the name suggest, these pre-selections are applied before topological selections are used and reduce the computational load and required storage by disregarding certain D^{*+} candidates. In the distributions of the cosine pointing angle (Figure 21) and normalised decay length (Figure 24) the effect of the pre-selections are also visible in the first four p_T intervals.
The tight $d_{0,K}$ cuts are chosen such that the selected fraction of feed-down D^{*+} is around 0.2 for each p_T region. In comparison with the loose cuts this will increase the prompt rejection. As shown in the right panel of Figure 17, only $3 - 10\%$ of the prompt D^{*+} is selected with the tight $d_{0,K}$ cuts.

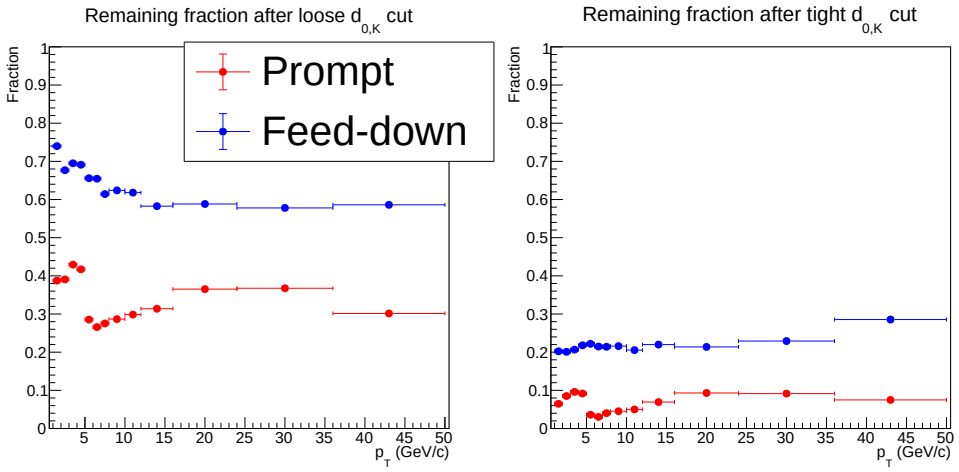

Figure 17: Estimation of the selected fraction of prompt ($N^{\text{after cut}}_{\text{prompt}}/N_{\text{prompt}}$) and feed-down ($N^{\text{after cut}}_{\text{feed-down}}/N_{\text{feed-down}}$) are shown for the loose and tight $d_{0,K}$ cuts in respectively the left and right panel.

4.2 Impact parameter pion

Similarly to the kaon impact parameter the distributions of the pion impact parameter are presented in Figure 18 and the ratios in Figure 19. A comparison of the kaon and pion impact parameter distributions is located in Appendix A.

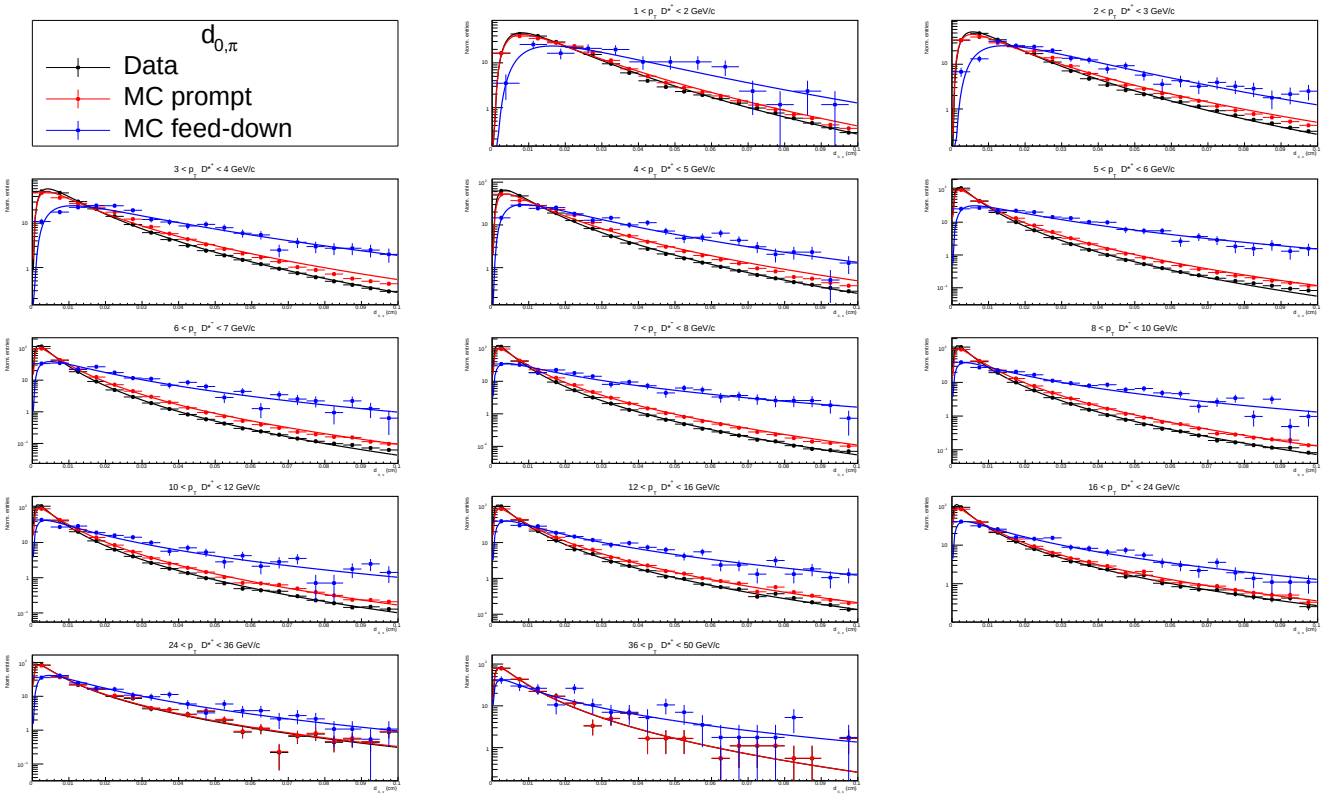

Figure 18: Normalised impact parameter pion ($d_{0,\pi}$) distributions for data (black), MC prompt (red) and MC feed-down (blue), separated in 13 D^{*+} p_T intervals. Y-axis has logarithmic scale. Fitted with log-normal distribution. The MC feed-down distributions are broader and shifted to the right compared to the MC prompt distributions.

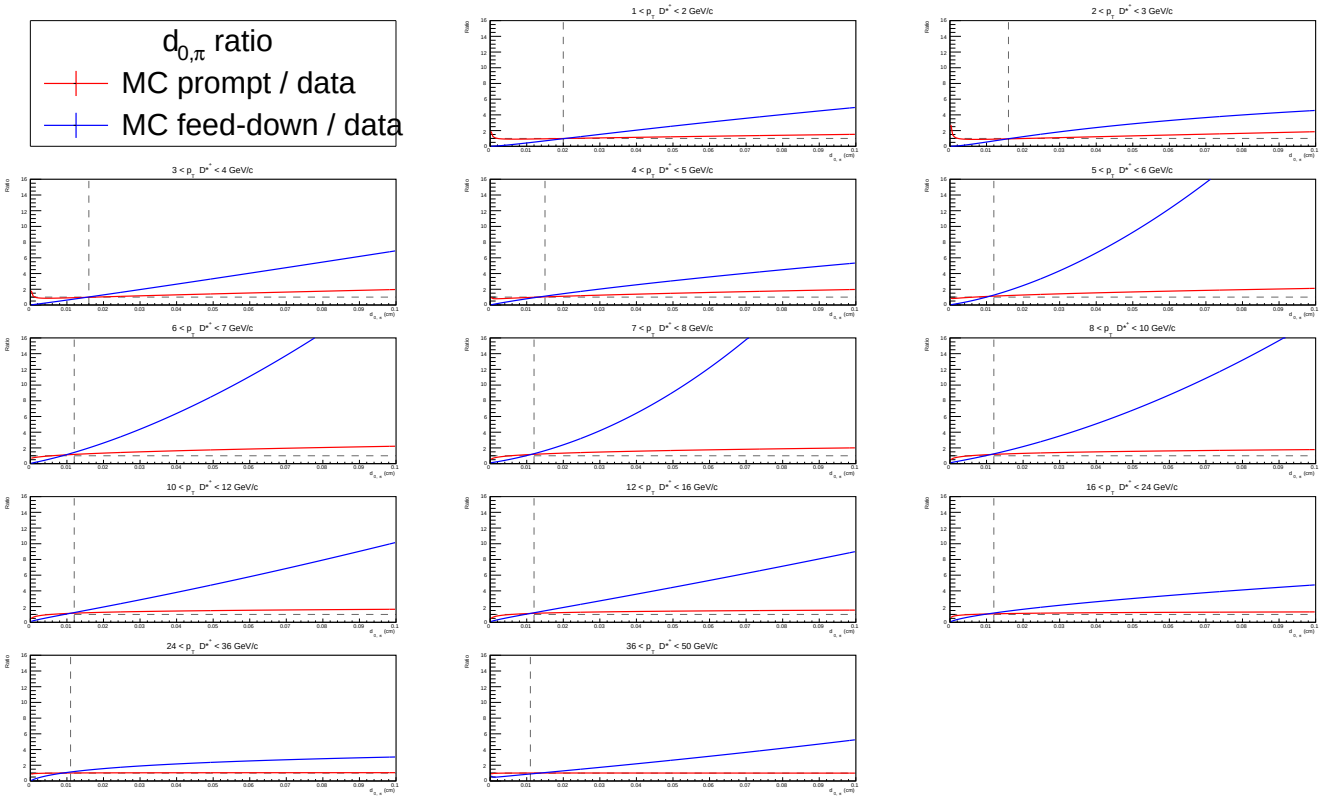

Figure 19: Ratios of the impact parameter pion ($d_{0,\pi}$) fits: $\frac{\text{MC prompt}}{\text{data}}$ (red) and $\frac{\text{MC feed-down}}{\text{data}}$ (blue). Separated in 13 D^{*+} p_T intervals. The intersections are between $0.01 - 0.02$ cm and for larger $d_{0,K}$ the $\frac{\text{MC feed-down}}{\text{data}}$ ratio becomes dominant. These intersections of the ratios are used as value for the loose cuts and are indicated with a vertical dashed line.

The loose and tight $d_{0,\pi}$ cuts are determined in exactly the same way as the $d_{0,K}$ cuts. Loose cuts at the intersection of the $\frac{\text{MC prompt}}{\text{data}}$ and $\frac{\text{MC feed-down}}{\text{data}}$ ratios. Tight cuts chosen such that $\sim 20\%$ of all feed-down D^{*+} is selected in each p_T interval. The estimated fraction of selected prompt and selected feed-down D^{*+}, after the loose and tight $d_{0,pi}$ cuts, are shown in respectively the left and right panel of Figure 20.

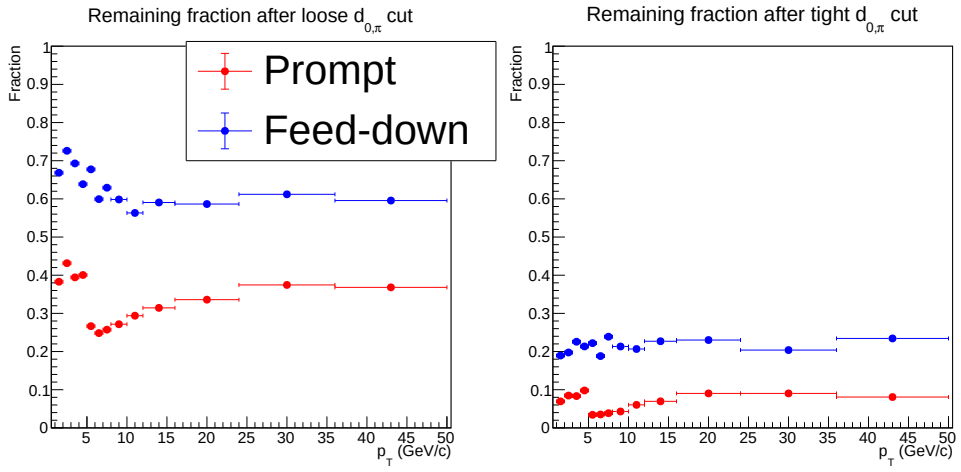

Figure 20: Estimation of the selected fraction of prompt ($N^{\text{after cut}}_{\text{prompt}}/N_{\text{prompt}}$) and feed-down ($N^{\text{after cut}}_{\text{feed-down}}/N_{\text{feed-down}}$) are shown for the loose and tight $d_{0,\pi}$ cuts in respectively the left and right panel.

4.3 Cosine pointing angle

The fitted Cosine pointing angle ($\cos(\theta_{point})$) distributions for data, MC prompt and MC feed-down are shown in Figure 21. Note that the the distributions in the first four p_T intervals do not have any entries below ~ 0.9. This is caused by the applied pre-selections. For high p_T the number of entries, especially for MC feed-down, is reduced. In particular in the last two p_T regions, the number of data points is smaller and the uncertainties are larger. As a result the fits deviate in comparison to the lower p_T intervals.

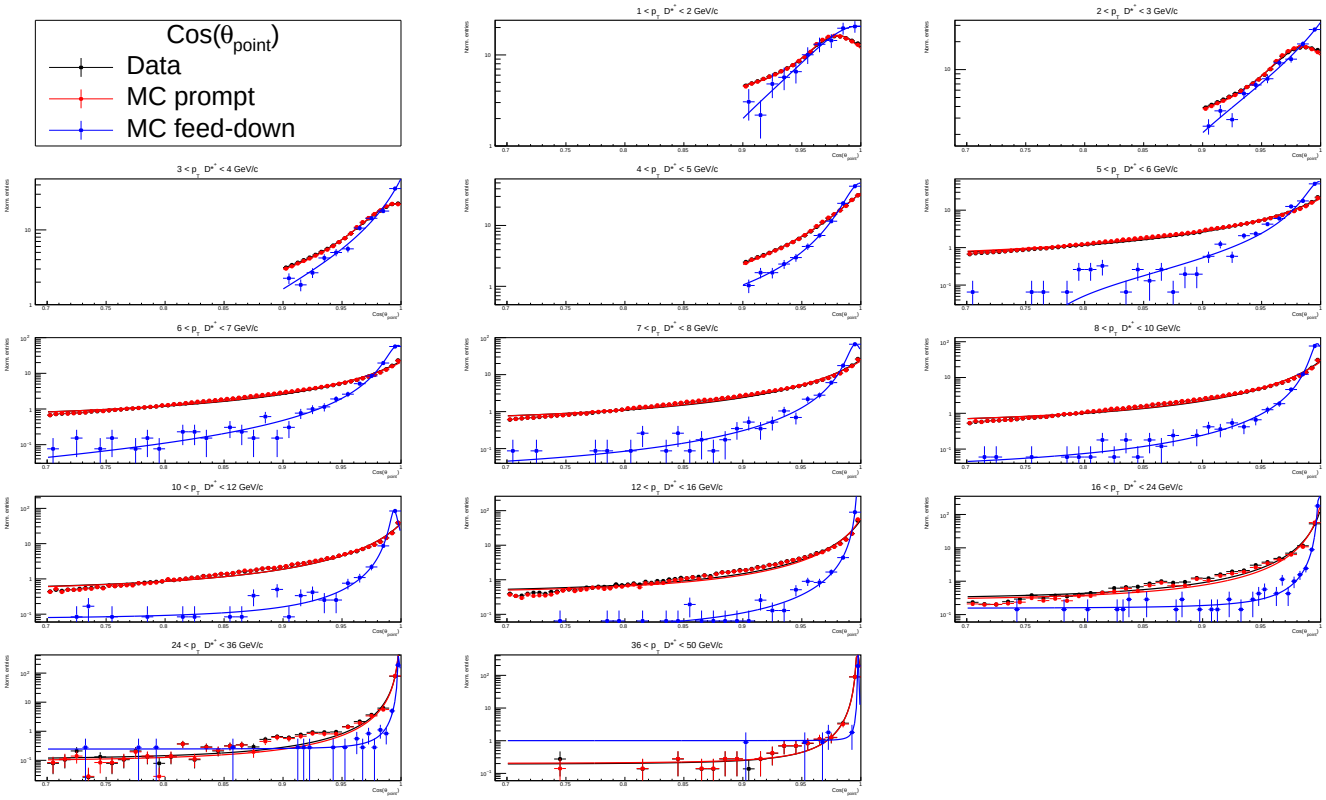

Figure 21: Cosine pointing angle ($\cos(\theta_{point})$) distributions for data (black), MC prompt (red) and MC feed-down (blue), separated in 13 D^{*+} p_T intervals. Y-axis has logarithmic scale. Fitted with BreitWigner distribution. In the first four p_T intervals there are no entries below ~ 0.9, this is because of the applied pre-selections. For high p_T (particularly the last three p_T intervals) the number of MC feed-down entries decreases significantly, which results in lower statistics and consequently less optimal fits.

The $\frac{\text{MC prompt}}{\text{data}}$ and $\frac{\text{MC feed-down}}{\text{data}}$ ratios of the $\cos(\theta_{point})$ distributions are shown in Figure 22. The intersections are located close to one. To increase the feed-down contribution it is desired to select the region between the intersection and 1, where $\frac{\text{MC feed-down}}{\text{data}} > \frac{\text{MC prompt}}{\text{data}}$. These selection regions are quiet small, especially for the higher p_T intervals, and are therefore used in both the loose and tight set of cuts. Because of the lower statistics for MC feed-down at high p_T, the fits of the MC feed-down distribution and consequently the ratio $\frac{\text{MC feed-down}}{\text{data}}$ are less than optimal. As a result no cut value can be determined using the ratio intersection for the last two p_T intervals. Instead the cuts for the last two p_T intervals are chosen to be the same as in interval $16 < p_T < 24$.

The fraction of prompt ($N^{\text{after cut}}_{\text{prompt}}/N_{\text{prompt}}$) and fraction of feed-down ($N^{\text{after cut}}_{\text{feed-down}}/N_{\text{feed-down}}$) selected using these $\cos(\theta_{point})$ cuts is estimated for each p_T interval in Figure 23.

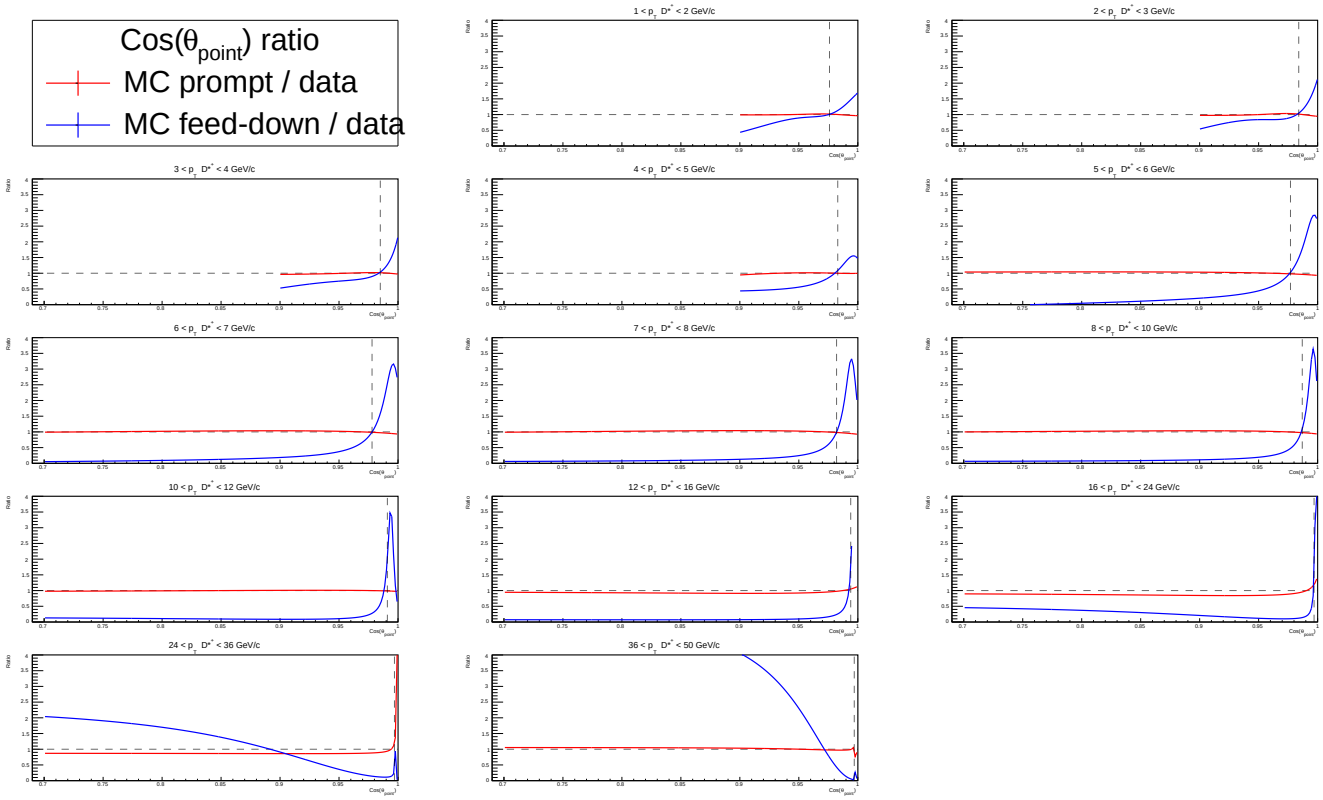

Figure 22: Ratios of the cosine pointing angle ($\cos(\theta_{point})$) fits: $\frac{\text{MC prompt}}{\text{data}}$ (red) and $\frac{\text{MC feed-down}}{\text{data}}$ (blue). Separated in 13 D^{*+} p_T intervals. For the last two p_T intervals no cut value can be determined using the ratio intersection. Instead the cuts for the last two p_T intervals are chosen to be the same as in interval $16 < p_T < 24$. The cut values determined here are used for both the loose and tight cuts. Cuts are indicated with vertical dashed line.

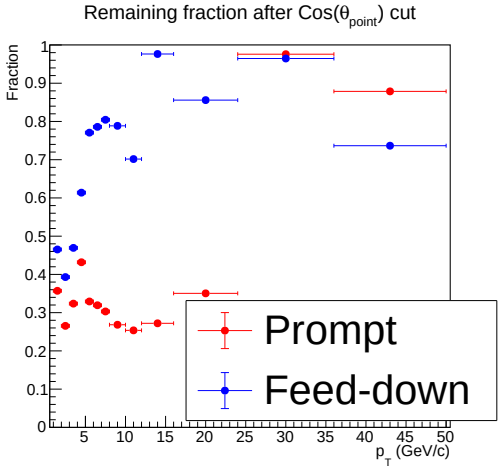

Figure 23: Estimation of the selected fraction of prompt ($N^{\text{after cut}}_{\text{prompt}}/N_{\text{prompt}}$) and feed-down ($N^{\text{after cut}}_{\text{feed-down}}/N_{\text{feed-down}}$) are shown for the $\cos(\theta_{point})$ cuts.

4.4 Normalised decay length XY

The normalised decay length XY distributions, fitted with Landau distributions modified with an exponential term, are shown in Figure 24. Note that the the distributions in the first four p_T intervals do not have any entries below ~ 2.5, and that the distributions in the fifth p_T interval ($5-6$ GeV/c) have a discontinuity at ~ 2.5. This is because of the applied pre-selections. The $\frac{\text{MC prompt}}{\text{data}}$ and $\frac{\text{MC feed-down}}{\text{data}}$ ratios of the Norm L_{XY} distributions are shown in Figure 25.

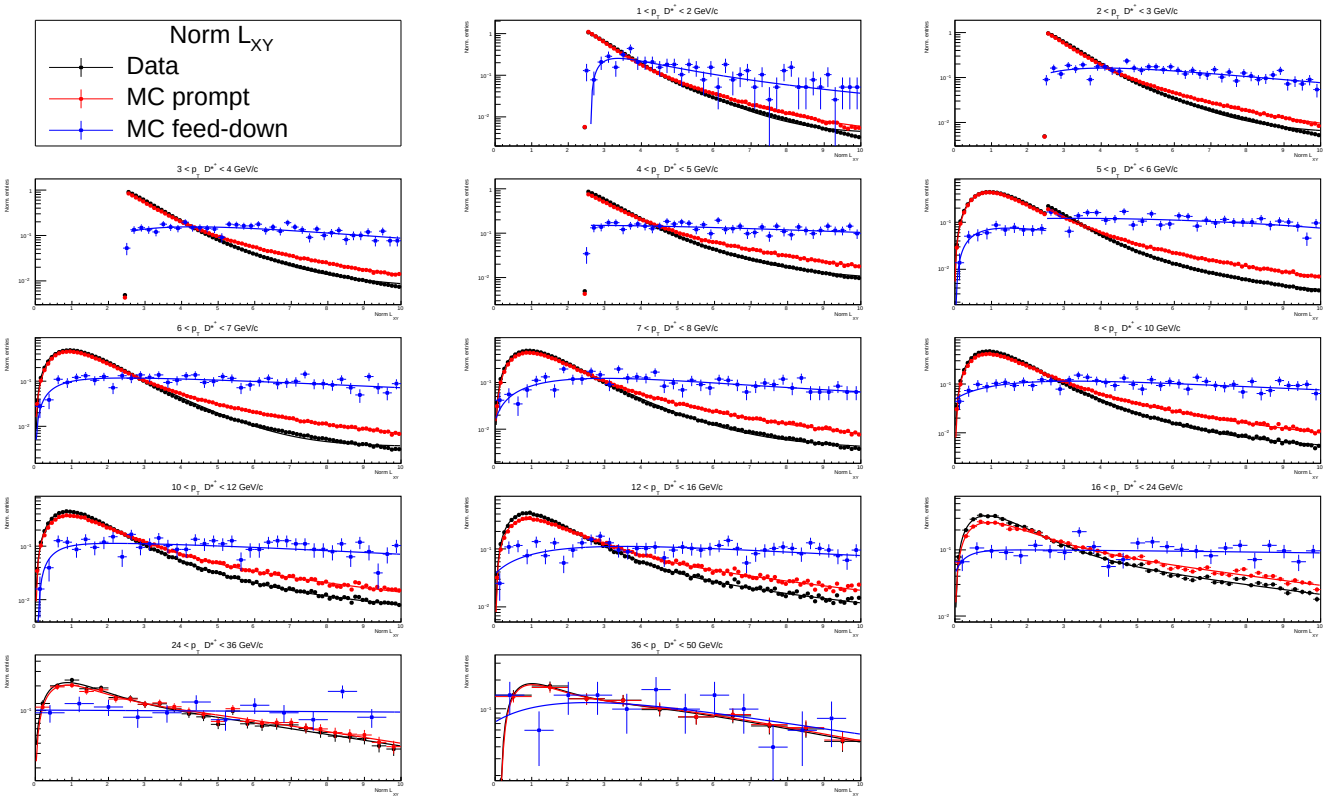

Figure 24: Normalised decay length XY (Norm L_{XY}) distributions for data (black), MC prompt (red) and MC feed-down (blue), separated in 13 D^{*+} p_T intervals. Y-axis has logarithmic scale. Fitted with landau distribution modified with an exponential term. No entries below ~ 2.5 in the first four p_T intervals and the discontinuities in the fifth p_T interval are caused by the applied pre-selections. MC prompt distributions are peaked around Norm $L_{XY} \approx 1$, while the MC feed-down distributions are more flat.

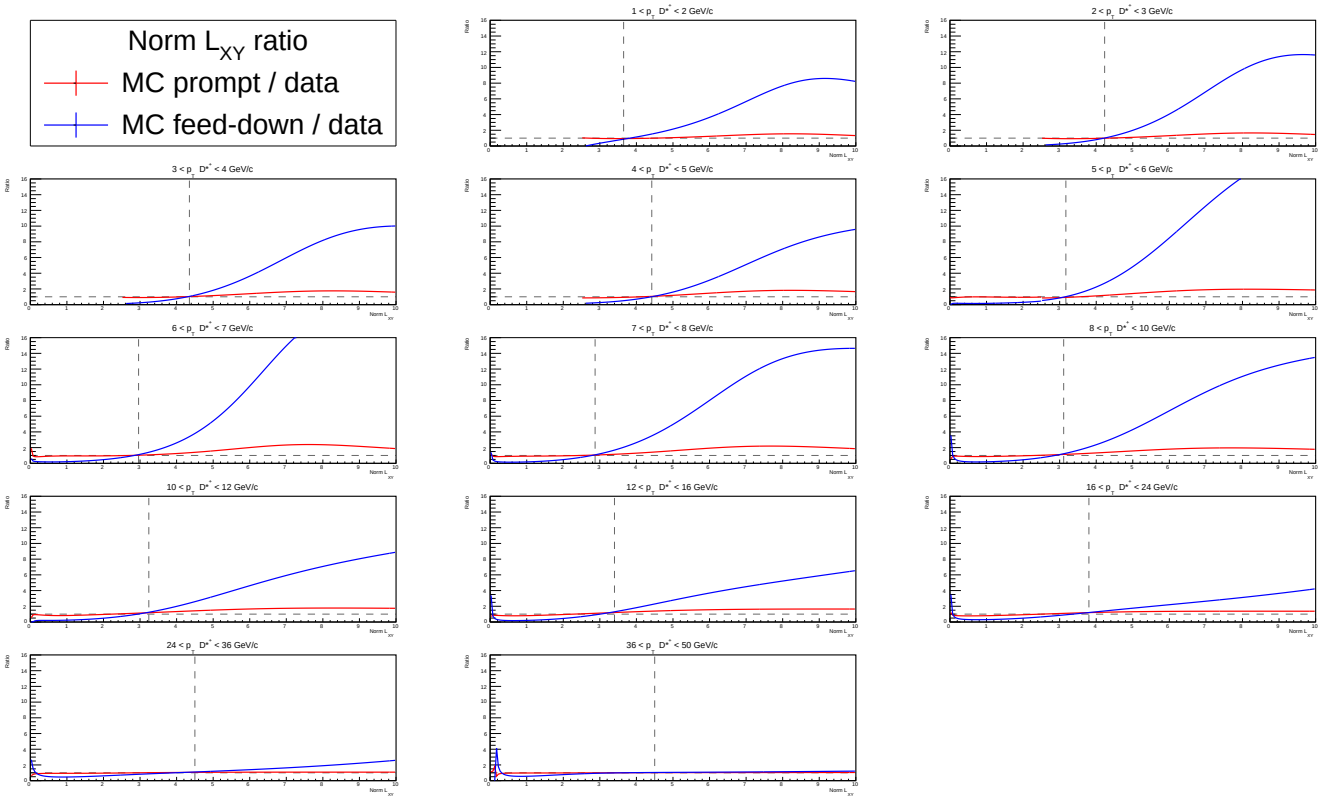

Figure 25: Ratios of the normalised decay length XY (Norm L_{XY}) fits: $\frac{\text{MC prompt}}{\text{data}}$ (red) and $\frac{\text{MC feed-down}}{\text{data}}$ (blue). Separated in 13 D^{*+} p_T intervals. The intersection of these ratios is used as value for the loose cuts and are indicated with a vertical dashed line.

The intersections of the $\frac{\text{MC prompt}}{\text{data}}$ and $\frac{\text{MC feed-down}}{\text{data}}$ ratios are used as value for the loose Norm L_{XY} cuts. The tight Norm L_{XY} cuts are determined such that the selected fraction of feed-down D^{*+} ($N^{\text{after cut}}_{\text{feed-down}}/N_{\text{feed-down}}$) is around 0.4 for each p_T region. As a result the estimated percentage of prompt for the tight cuts is between $5-35\%$, depending on p_T.

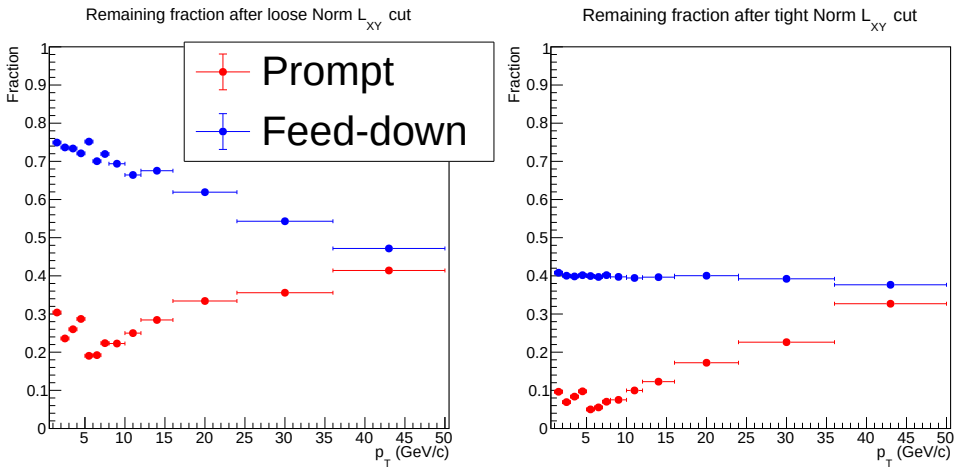

Figure 26: Estimation of the selected fraction of prompt ($N^{\text{after cut}}_{\text{prompt}}/N_{\text{prompt}}$) and feed-down ($N^{\text{after cut}}_{\text{feed-down}}/N_{\text{feed-down}}$) are shown for the loose and tight Norm L_{XY} cuts in respectively the left and right panel.

4.5 Tables of topological cuts

The $d_{0,K}$, $d_{0,\pi}$, $\cos(\theta_{point})$ and Norm L_{XY} topological cuts determined in the previous subsections are summarised in the following tables. Values for the standard analysis, which will be used for comparison, are reported in Table 2. The loose and tight feed-down enhanced cuts are presented in respectively Table 3 and Table 4. Note that for $\cos(\theta_{point})$ the feed-down enhanced loose and tight cuts are equivalent. A difference between the standard and feed-down enhanced cuts is that for the impact parameters the standard analysis has lower cuts ($<$), while the feed-down enhanced cuts have upper cuts ($>$).

Table 2: Standard analysis selections for topological variables: impact parameter kaon and pion, normalised decay length XY and cosine pointing angle.

$p_T\,(GeV/c)$	$[1,2]$	$[2,3]$	$[3,4]$	$[4,5]$	$[5,6]$	$[6,7]$	$[7,8]$	$[8,10]$	$[10,12]$	$[12,16]$	$[16,24]$	$[24,36]$
$d_{0,K}\,(cm)$	< 0.1	< 0.1	< 0.1	< 0.1	< 0.1	< 0.1	< 0.1	< 0.12	< 0.12	< 0.15	< 0.15	< 0.2
$d_{0,\pi}\,(cm)$	< 0.1	< 0.1	< 0.1	< 0.1	< 0.1	< 0.1	< 0.1	< 0.12	< 0.12	< 0.15	< 0.15	< 0.2
$Norm\,L_{XY}$	> 7.5	> 7.5	> 7.5	> 6.5	> 6.5	> 6.5	> 6	> 5	> 5	> 3.7	> 2	> 0
$\cos(\theta_{point})$	> 0.99	> 0.98	> 0.98	> 0.96	> 0.93	> 0.93	> 0.92	> 0.92	> 0.92	> 0.92	> 0.92	> 0.85

Table 3: Loose feed-down enhanced selections for topological variables: impact parameter kaon and pion, normalised decay length XY and cosine pointing angle.

$p_T\,(GeV/c)$	$[1,2]$	$[2,3]$	$[3,4]$	$[4,5]$	$[5,6]$	$[6,7]$	$[7,8]$	$[8,10]$	$[10,12]$	$[12,16]$	$[16,24]$	$[24,36]$
$d_{0,K}\,(cm)$	> 0.020	> 0.018	> 0.015	> 0.015	> 0.012	> 0.012	> 0.012	> 0.012	> 0.012	> 0.012	> 0.011	> 0.011
$d_{0,\pi}\,(cm)$	> 0.020	> 0.016	> 0.016	> 0.015	> 0.012	> 0.012	> 0.012	> 0.012	> 0.012	> 0.012	> 0.012	> 0.011
$Norm\,L_{XY}$	> 3.65	> 4.23	> 4.35	> 4.42	> 3.17	> 2.96	> 2.87	> 3.11	> 3.24	> 3.40	> 3.80	> 4.50
$\cos(\theta_{point})$	> 0.976	> 0.984	> 0.985	> 0.983	> 0.977	> 0.978	> 0.982	> 0.987	> 0.991	> 0.994	> 0.997	> 0.997

Table 4: Tight feed-down enhanced selections for topological variables: impact parameter kaon and pion, normalised decay length XY and cosine pointing angle.

$p_T\,(GeV/c)$	$[1,2]$	$[2,3]$	$[3,4]$	$[4,5]$	$[5,6]$	$[6,7]$	$[7,8]$	$[8,10]$	$[10,12]$	$[12,16]$	$[16,24]$	$[24,36]$
$d_{0,K}\,(cm)$	> 0.052	> 0.048	> 0.045	> 0.045	> 0.041	> 0.041	> 0.038	> 0.038	> 0.038	> 0.035	> 0.035	> 0.035
$d_{0,\pi}\,(cm)$	> 0.050	> 0.047	> 0.047	> 0.042	> 0.041	> 0.038	> 0.038	> 0.038	> 0.035	> 0.035	> 0.035	> 0.035
$Norm\,L_{XY}$	> 5.19	> 6.34	> 6.53	> 6.67	> 6.00	> 5.60	> 5.42	> 5.70	> 5.64	> 5.83	> 5.93	> 6.01
$\cos(\theta_{point})$	> 0.976	> 0.984	> 0.985	> 0.983	> 0.977	> 0.978	> 0.982	> 0.987	> 0.991	> 0.994	> 0.997	> 0.997

For the 12 other topological variables (mentioned in Section 2.6) the values presented in Table 5 are used. In this study the values for these topological variables are not specifically optimised for feed-down selection.

Table 5: Values for the D^{*+} topological selection variables, excluding: impact parameter kaon and pion, normalised decay length XY and cosine pointing angle. These cuts are used for the standard analysis, as well as both the feed-down enhanced cuts.

$p_T\,(GeV/c)$	$[1,2]$	$[2,3]$	$[3,4]$	$[4,5]$	$[5,6]$	$[6,7]$	$[7,8]$	$[8,10]$	$[10,12]$	$[12,16]$	$[16,24]$	$[24,36]$	$[36,50]$
$\Delta M_{D^0}\,(GeV)$	< 0.024	< 0.024	< 0.024	< 0.03	< 0.03	< 0.034	< 0.036	< 0.055	< 0.055	< 0.074	< 0.074	< 0.094	< 0.094
$DCA\,(cm)$	< 0.022	< 0.022	< 0.022	< 0.021	< 0.02	< 0.02	< 0.02	< 0.02	< 0.02	< 0.02	< 0.02	< 0.02	< 0.02
$\cos(\theta^*)$	< 0.8	< 0.8	< 0.8	< 0.8	< 1	< 1	< 1	< 1	< 1	< 1	< 1	< 1	< 1
$p_T(K)\,(GeV/c)$	> 0.8	> 0.8	> 1	> 0.8	> 0.8	> 0.8	> 0.8	> 0.7	> 0.7	> 0.7	> 0.5	> 0.5	> 0.5
$p_T(\pi)\,(GeV/c)$	> 1	> 1	> 1	> 1	> 1	> 1	> 1	> 0.9	> 0.7	> 0.7	> 0.5	> 0.5	> 0.5
$d_{0,K} \times d_{0,\pi}\,(cm^2)$	< -0.0004	< -0.0004	< -0.00035	< -0.00035	< -0.00023	< -0.0002	< -0.00015	$< -7.5e-05$	$< -7.5e-05$	$< -7.5e-05$	$< -7.5e-05$	< 0.0004	< 0.0004
inv. mass half width of $D^*\,(GeV)$	< 0.3	< 0.3	< 0.3	< 0.3	< 0.3	< 0.3	< 0.3	< 0.3	< 0.3	< 0.3	< 0.3	< 0.15	< 0.15
half width of $M_{K\pi\pi} - M_{D^0}\,(GeV)$	< 0.15	< 0.15	< 0.15	< 0.15	< 0.15	< 0.15	< 0.15	< 0.15	< 0.15	< 0.15	< 0.15	< 0.15	< 0.15
min $p_T(\pi_s)\,(GeV/c)$	< 0.05	< 0.05	< 0.05	< 0.05	< 0.2	< 0.3	< 0.3	< 0.3	< 0.3	< 0.3	< 0.3	< 0.3	< 0.3
max $p_T(\pi_s)\,(GeV/c)$	< 0.5	< 0.5	< 0.5	< 10	< 10	< 100	< 100	< 100	< 100	< 100	< 100	< 100	< 100
angle $\pi_s - D_0$ decay plane (rad)	> 1	> 1	> 1	> 1	> 1	> 1	> 1	> 1	> 1	> 1	> 1	> 1	> 1
$\cos(\theta_{point})_{XY}$	> 0.998	> 0.998	> 0.998	> 0.998	> 0.998	> 0.998	> 0.998	> 0.998	> 0.998	> 0.99	> 0.99	> 0.9	> 0.9

4.6 Invariant mass spectra

The invariant mass spectra from the standard analysis (Table 2 + Table 5) are shown in Figure 27 for each p_T interval. The spectra resulting from applying the loose (Table 3 + Table 5) and tight (Table 4 + Table 5) feed-down enhanced cuts are presented in respectively Figure 28 and Figure 29.

For all three sets of cuts the best significance is obtained at intermediate transverse momentum (p_T D^{*+}). For low p_T and high p_T the significance is lower because of respectively the larger combinatorial background and poorer statistics. The loose topological cuts select smaller regions compared to the standard analysis and as a result the number of entries are lower. The tight cuts select even smaller regions, resulting in even fewer entries. Significant D^{*+} signals are present for the loose cuts between $4-24$ GeV/c.
Some of the p_T intervals of the tight cut mass spectra are combined to increase the significance of the D^{*+} signal. As a result D^{*+} signals are visible between $2-8$ GeV/c. The significancies of these peaks are not very large ($2.6-2.8$) and have relatively large uncertainties ($1.2-1.5$).

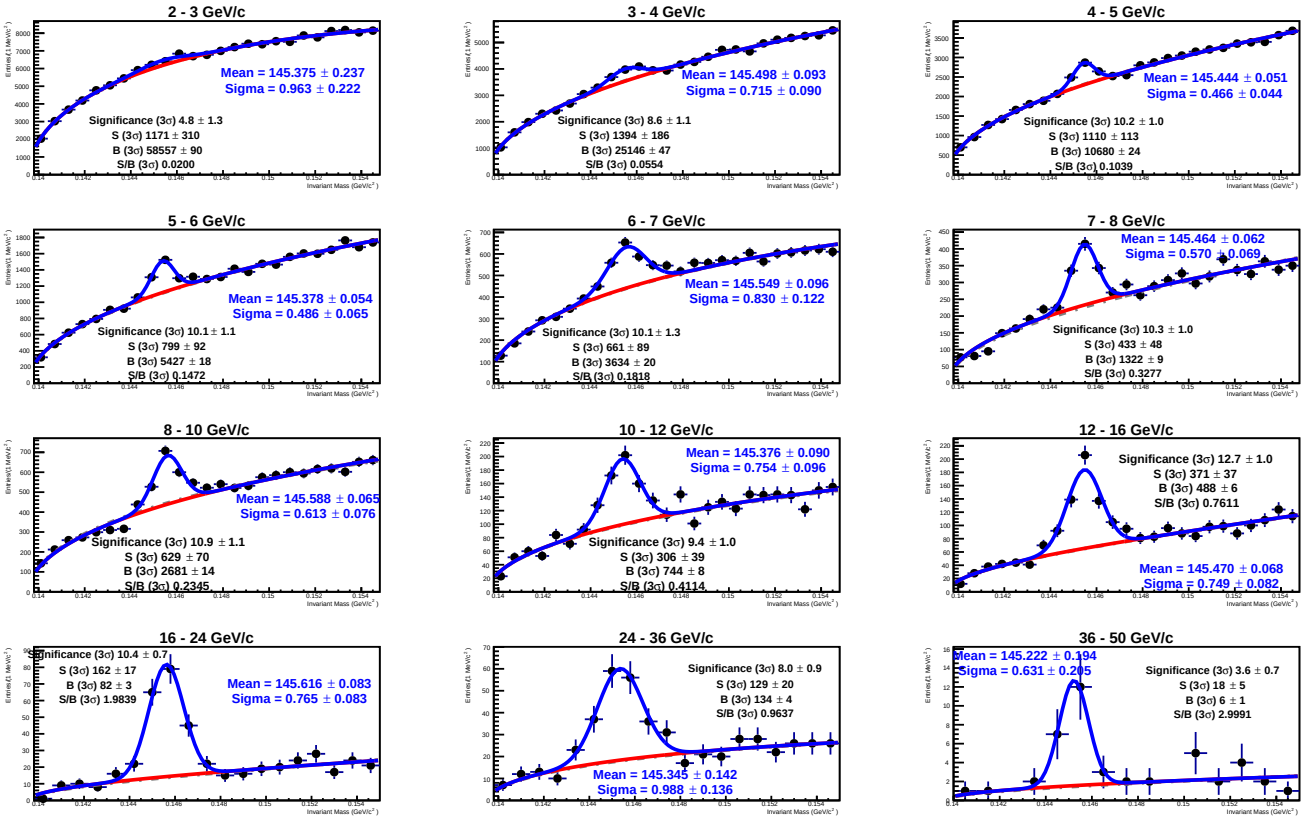

Figure 27: Invariant-mass spectra for 12 transverse momentum intervals, obtained by applying the standard analysis cuts reported in Table 2 and Table 5. The mass spectrum for $1 < p_T < 2$ GeV/c is not displayed because no significant peak was present above the background. The best significance is obtained at intermediate p_T D^{*+}.

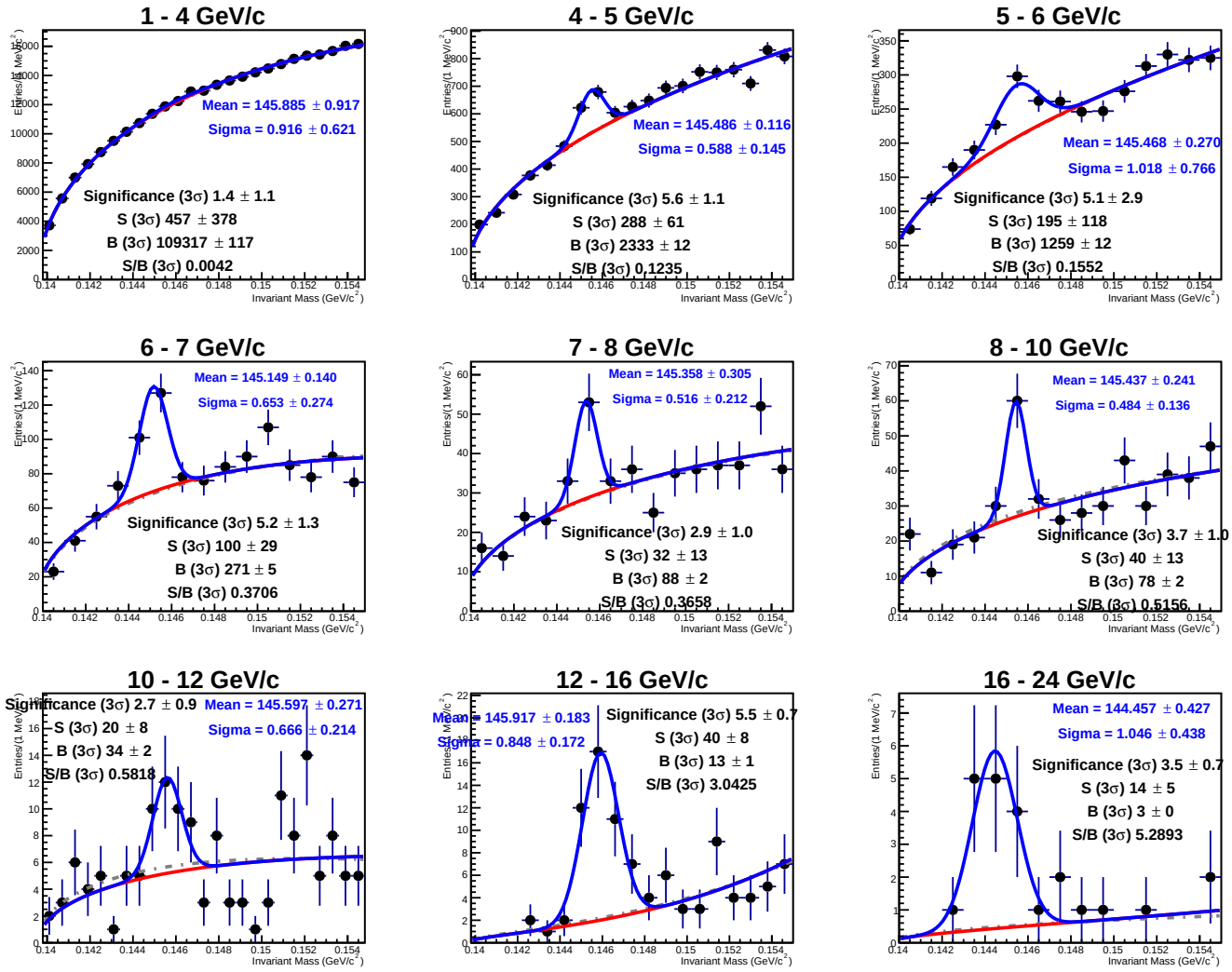

Figure 28: Invariant-mass spectra obtained by applying the set of loose feed-down enhanced topological cuts reported in Table 3 and the cuts in Table 5. For low p_T (< 4 GeV/c) spectra no significant signal is present above the background. For $p_T > 24$ GeV/c no significant signal is present in the spectra due to poor statistics.

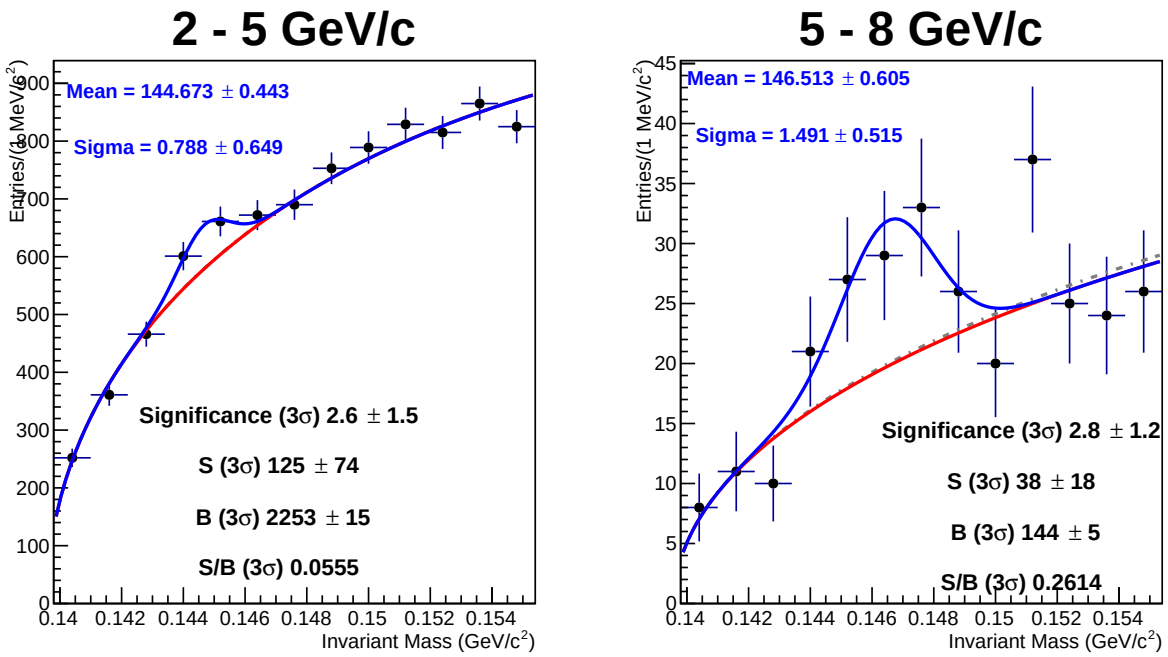

Figure 29: Invariant-mass spectra obtained by applying the set of tight feed-down enhanced topological cuts reported in Table 4 and the cuts in Table 5. For $p_T < 2$ and $p_T > 8$ GeV/c no mass spectra are presented because of the absence of significant signals and low statistics. To achieve higher statistics between $2 - 8$ GeV/c mass spectra a combined into 2 larger p_T intervals.

4.7 Efficiency

The efficiency in each of the 13 p_T intervals of the three sets of cuts are reported in Figure 30. The feed-down efficiency of the standard analysis and feed-down enhanced cuts are comparable. With exception of the first p_T interval the efficiencies deviate up to 15%. On the other hand, the prompt efficiency of the feed-down enhanced cuts compared to the standard analysis is larger at low p_T (< 8 GeV/c) and smaller at high p_T (> 24 GeV/c).

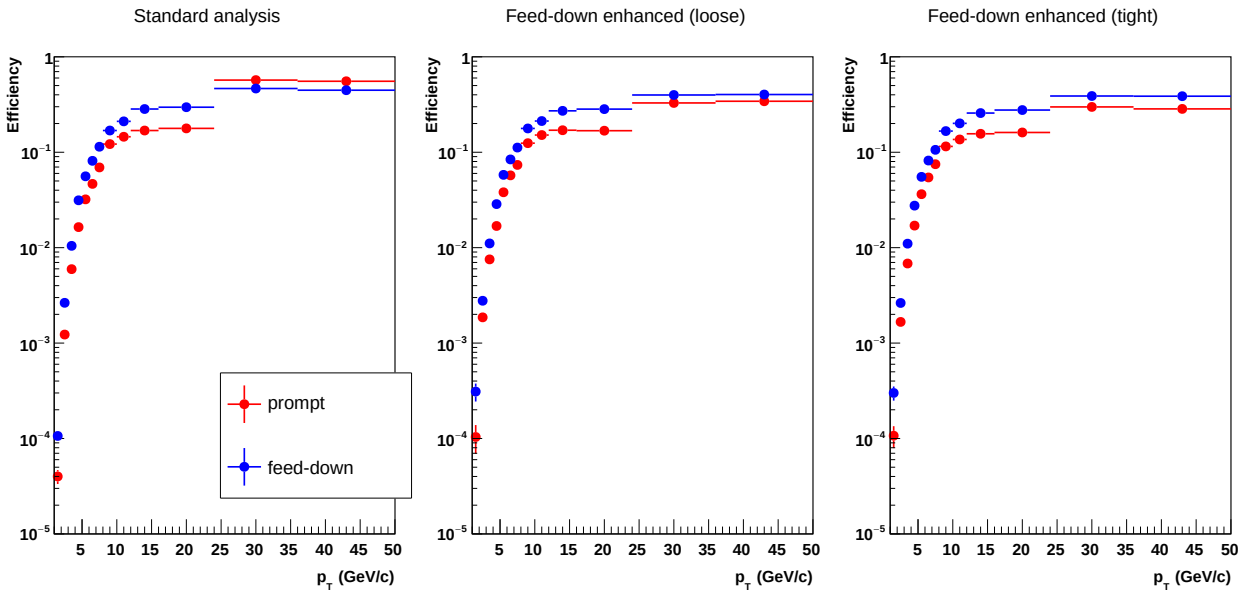

Figure 30: Prompt (red) and feed-down (blue) efficiency, as a function of p_T, of the prompt enhanced cuts (left), loose feed-down enhanced cuts (center) and tight feed-down enhanced cuts (right).

4.8 Prompt fraction

In Figure 31 the prompt fraction of the standard analysis (black), loose (red) and tight (blue) feed-down enhanced cuts are displayed. The standard analysis has a high prompt fraction of around $90 - 95\%$.

In the invariant mass spectra resulting of the loose feed-down enhanced cuts (Figure 28) the D^{*+} signal is only significant in the p_T intervals between $4 - 24$ GeV/c. Consequently the prompt fractions for the loose cuts are only calculated in this p_T region. These prompt fractions are between $0.5 - 0.9\%$ and indicate an decrease in f_{prompt} as p_T increases. Compared to the standard analysis, the prompt fractions of the loose feed-down enhanced cuts are much smaller. In interval $10 < p_T < 12$ GeV/cm, for example, the prompt fractions is $\sim 55\%$, meaning that the amount of selected prompt and feed-down D^{*+} is approximately equal.

For the tight feed-down enhanced cuts the prompt fractions are calculated for the same two p_T intervals as used for the invariant mass spectra (Figure 29). In interval $2 < p_T < 5$ GeV/c and $5 < p_T < 8$ GeV/c the prompt fractions are respectively ~ 0.75 and ~ 0.1. As expected the tight feed-down enhanced cuts result in higher prompt rejection compared to the loose feed-down enhanced cuts.

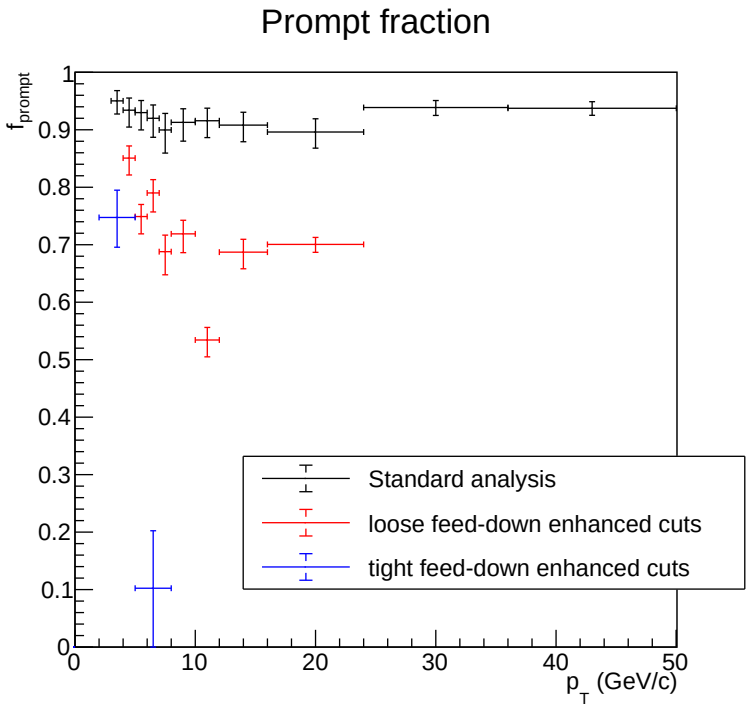

Figure 31: Prompt fraction (f_{prompt}) as a function of p_T for the standard analysis (black) and loose feed-down enhanced cuts (red) and tight feed-down enhanced cuts (blue).

In Table 6 and Table 7 the purity of respectively the loose and tight feed-down enhanced cuts are tabulated.

Table 6: Purity ($N^{\mathrm{D}^{*+}}_{\text{feed-down}}/N^{\mathrm{D}^{*+}}$) of loose feed-down enhanced selections.

$p_T\,(GeV/c)$	Purity
$[4,5]$	$15^{+2.9}_{-2.1}$ %
$[5,6]$	$25^{+3.0}_{-2.1}$ %
$[6,7]$	$21^{+3.3}_{-2.3}$ %
$[7,8]$	$31^{+4.0}_{-2.9}$ %
$[8,10]$	$28^{+3.3}_{-2.4}$ %
$[10,12]$	$47^{+2.9}_{-2.2}$ %
$[12,16]$	$31^{+2.9}_{-2.2}$ %
$[16,24]$	$30^{+1.4}_{-1.2}$ %

Table 7: Purity ($N^{\mathrm{D}^{*+}}_{\text{feed-down}}/N^{\mathrm{D}^{*+}}$) of tight feed-down enhanced selections.

$p_T\,(GeV/c)$	Purity
$[2,5]$	$25^{+5.2}_{-4.7}$ %
$[5,8]$	90^{+15}_{-10} %

5 Conclusion and discussion

In this thesis the selection of feed-down D^{*+} using topological selection variables was studied. The topological selection variables investigated are: impact parameter kaon, impact

parameter pion, normalised decay length XY and cosine pointing angle. For these four selection variables two sets of D^{*+} feed-down enhanced cuts are reported: a set of loose cuts (Table 3) and a set of tight cuts (Table 4). Both sets of cuts are aimed at increasing the contribution of feed-down D^{*+}, but the loose cuts are tailored for higher signals, while the tight cuts are determined with higher prompt rejection in mind. The loose and tight sets of feed-down enhanced cuts were individually applied to Pb-Pb collision data from ALICE ($\sqrt{s_{NN}} = 5.02$ TeV, centrality class 10-30%) and compared to the standard analysis.

The invariant mass spectra show that both sets of feed-down enhanced cuts are proficient at selecting real D^{*+} in certain transverse momentum regions. Significant D^{*+} signals are present for the loose cuts at $4 < p_T < 24$ GeV/c and for the tight cuts at $2 < p_T < 8$ GeV/c. At lower p_T no significant signals are present as a result of the large combinatorial background dominating the real D^{*+} signal. At higher p_T the significance is lower because of poorer statistics. Compared to the standard analysis, the D^{*+} signal is visible in a smaller p_T range and the significancies are lower. This is expected since the feed-down enhanced cuts cut away a large number of the more abundant prompt D^{*+}. The mass spectra of the tight feed-down enhanced cuts have no significant signals at $p_T > 8$ GeV/c, because of the too tight cuts cutting away almost all D^{*+}.

The efficiency of the loose feed-down enhanced cuts is similar to the efficiency of the standard analysis at intermediate p_T. At low p_T (< 2 GeV/c) however the prompt and feed-down efficiency is worse and at high p_T (> 24 GeV/c) the prompt efficiency is lower for the loose cuts.

The prompt fractions resulting from the loose feed-down enhanced cuts are between $50-90\%$ depending on the p_T interval. In comparison to the prompt fractions of the standard analysis, which are around 95%, the prompt fractions for the loose feed-down enhanced cuts show a desired increase in feed-down contribution.

For the tight feed-down enhanced cuts the prompt fraction in interval $2 < p_T < 5$ GeV/c is ~ 0.75, indicating a moderate increase in prompt rejection compared to the standard analysis. The prompt fraction in the interval $5 < p_T < 8$ GeV/c is much smaller, around 10%. This means that the feed-down contribution is very large, in fact similar to the prompt contribution in the standard analysis. In this interval the invariant mass spectrum shows a D^{*+} signal (significance 2.8 ± 1.2). This indicates that the tight feed-down enhanced cuts can be used to select feed-down D^{*+} with high purity ($\sim 90\%$) in the region $5 < p_T < 8$ GeV/c. For higher p_T the chosen cuts are too tight resulting in the loss of significant signals.

From the results of the tight cuts in region $5 < p_T < 8$ GeV/c it can be concluded that exploiting the different shapes of the topological variable distributions is a viable method for selecting samples of feed-down D^{*+} with high purity. In this study high purity is only reached using the tight feed-down enhanced cuts in interval $5 < p_T < 8$ GeV/c and the corresponding mass spectrum shows relatively low significance. Further research should be performed to increase the p_T region and improve the statistics, possible future research will be presented in Section 6. When higher statistics (higher significancies and smaller uncertainties) are achieved, one could use the high purity feed-down D^{*+} to study beauty production. Having

access to charm quarks with the standard analysis and access to beauty quarks with the feed-down enhanced cuts allows for experimental research on the effect of mass on the energy loss in the QGP.

6 Outlook

The feed-down enhanced cuts reported in this thesis are able to select D^{*+} mesons with an larger feed-down contribution compared to the standard analysis. In this thesis two sets of cuts were presented, loose and tight. Additional research can be performed to determine intermediate cut values, which would be more proficient at rejecting prompt than the loose cuts, while also resulting in higher statistics and significance compared to the tight cuts presented in this thesis. In particular at high p_T, where the statistics are lower, using looser cuts could improve the statistics. In this study the same cosine pointing angle cuts where used for both the loose and tight cuts. Looser cuts on the $\cos(\theta_{point})$ could also be evaluated to improve the statistics. The statistics could also be improved further by using larger data samples, for example from the future LHC Run 3.

Only four topological variables were feed-down optimised in this study. To further improve the contribution of feed-down and rejection of prompt D^{*+}, feed-down enhanced cut values need to be determined for the other topological variables used (Section 2.6). Examples of topological variables that could be studied next are: product of kaon and pion impact parameter ($d_{0,K} \times d_{0.\pi}$) and cosine of pointing angle in xy-plane ($\cos(\theta_{point})_{XY}$). The correlation between the topological variables may also be studied to help with the determination of feed-down enhanced selection values.

References

[1] MissMJ, *Standard model of elementary particles*, 2006, https://en.wikipedia.org/wiki/Standard_Model#/media/File:Standard_Model_of_Elementary_Particles.svg (visited on 05/02/2018).

[2] R. de Rooij, "Prompt D*+ production in proton-proton and lead-lead collisions, measured with the ALICE experiment at the CERN Large Hadron Collider", PhD thesis (Utrecht University, 2013).

[3] E. Henley and A. Garcia, *Subatomic Physics* (World Scientific, 2007).

[4] F. Grosa, "Measurement of the prompt and feed-down contributions to the D+-meson production with the ALICE experiment at LHC", MA thesis (University of Turin, 2016).

[5] *The CERN accelerator complex*, https://cds.cern.ch/record/1621894 (visited on 05/21/2018).

[6] *The Large Hadron Collider*, https://home.cern/topics/large-hadron-collider (visited on 05/21/2018).

[7] *Experiments: A range of experiments at CERN investigate physics from cosmic rays to supersymmetry*, https://home.cern/about/experiments (visited on 05/23/2018).

[8] *ALICE — CERN*, https://home.cern/about/experiments/alice (visited on 05/23/2018).

[9] ALICE Collaboration, "The alice experiment at the cern lhc", Journal of Instrumentation **3**, S08002 (2008), http://stacks.iop.org/1748-0221/3/i=08/a=S08002.

[10] A. Tauro, *ALICE Schematic*, May 2017, https://cds.cern.ch/record/2263642 (visited on 06/04/2018).

[11] ALICE collaboration, "Alignment of the ALICE Inner Tracking System with cosmic-ray tracks", Journal of Instrumentation **5**, P03003 (2010), http://stacks.iop.org/1748-0221/5/i=03/a=P03003.

[12] *More details on the ALICE TPC*, http://alice.web.cern.ch/detectors/more-details-alice-tpc (visited on 05/23/2018).

[13] ALICE Collaboration, "Performance of the ALICE Experiment at the CERN LHC", International Journal of Modern Physics **29**, 1430044 (2014), https://arxiv.org/abs/1402.4476.

[14] *The ALICE Time of Flight Detector*, http://aliceinfo.cern.ch/Public/en/Chapter2/Chap2_TOF.html (visited on 05/24/2018).

[15] M. Tanabashi *et al.* (Particle Data Group), Phys. Rev. D **98**, 030001 (2018).

[16] *ROOT a Data analysis Framework*, https://root.cern.ch (visited on 05/14/2018).

[17] *ALICE Off-line*, http://alice-offline.web.cern.ch (visited on 05/14/2018).

[18] ALICE collaboration, "D meson nuclear modification factor in Pb-Pb collisions at $\sqrt{s_{NN}} = 5.02$ TeV in $0-10\%$, $30-50\%$ and $60-80\%$ centrality classes as a function of p_T.", in preparation.

A Comparison of kaon and pion impact parameter

In Figure 32 the normalised kaon and pion impact parameter distributions are compared. The kaon (K^-) has a mass more than three times that of the pion (π^+). This difference in mass may result in a difference in particle trajectory in the detectors magnetic field, and consequently a slightly altered impact parameter distribution. The plots in Figure 32 do not show a significant difference between the kaon and pion impact parameter distributions. Because of the short kaon/pion travel distance, it is possible that the difference in mass does not manifest in a large difference in impact parameter. Additionally the resolution of the detectors and the statistics may not be accurate enough to show this difference in a significant manner.

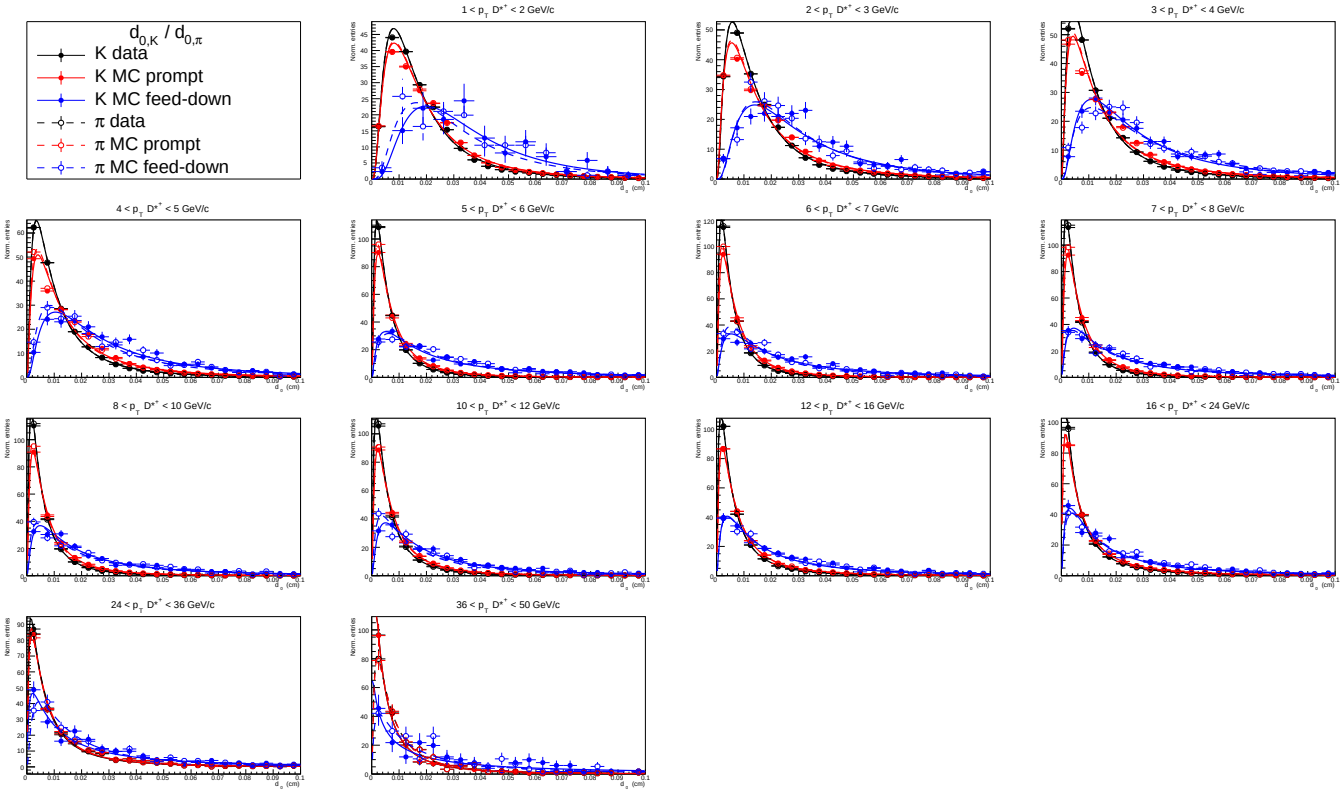

Figure 32: Normalised impact parameter kaon ($d_{0,K}$) and pion ($d_{0,\pi}$) distributions for data (black), MC prompt (red) and MC feed-down (blue), separated in 13 D^{*+} p_T intervals. $d_{0,K}$ is indicated with filled points and solid fit line. $d_{0,\pi}$ is indicated with open points and dashed fit. Log-normal distribution is used as fit function. Overall the kaon and pion impact parameter look very similar. MC feed-down distributions are broader (not as sharply peaked) and shifted to the right compared to the MC prompt distributions.